Fossilized silica diagenetic fronts: Implications for palaeoceanographic evolution across the Falkland/Malvinas plateau

Banafsheh Najjarifarizhendi [*], Gabriele Uenzelmann-Neben

Alfred-Wegener-Institute für Polar- und Meeresforschung, Am Alten Hafen 26, 27568, Bremerhaven, Germany

A B S T R A C T

A set of newly collected 2D seismic reflection data allows the mapping of two distinct cross-cutting reflectors across the Falkland/Malvinas Plateau. Reflector XR-F/MB in the Falkland/Malvinas Basin appears as a bottom simulating reflector that mimics the geometry of the present seafloor, whereas reflector XR-F/MT in the Falkland/Malvinas Trough is a non-bottom simulating reflector that mimics a shallower reflector representing the Early-Middle Miocene unconformity. The discordant geometry of these two reflectors with respect to the host-stratigraphy is argued to be associated with Opal-A to Opal-CT diagenesis, which is primarily a function of temperature. However, the estimated temperature at the present depth for reflector XR-F/MB lies below the minimum temperature for the onset of silica diagenesis. Based on their geometry and seismic characteristics, the two reflectors are interpreted to be fossilized silica diagenetic fronts, formed under palaeo-thermal conditions different from today. We hypothesize that the erosional action of intensified deep and bottom water masses subsequent to Antarctic glaciations during the Early-Middle Miocene may have driven the fossilization of the diagenetic front in the study area. It is estimated that erosion of a minimum of 270 m of overburden would account for the temperature drop driving the fossilization of the silica diagenetic fron.

1. Introduction

Cross-cutting reflectors of positive or negative polarity are distinctive features on seismic reflection profiles due to their discordance with host stratigraphic reflections (e.g. Berndt et al., 2004). Cross-cutting reflections may be a function of seafloor geometry (bottom simulating reflector, or BSR), or may show no geometrical similarity to the seafloor (non-bottom simulating, or NBSR) (Bohrmann et al., 1992; Berndt et al., 2004; Varkouhi et al., 2022). Cross-cutting reflectors are interpreted to be associated with secondary (post-depositional) geochemical processes, notably silica diagenesis or gas hydrate (GH) formation (Berndt et al., 2004; Shedd et al., 2012). These two processes involve very different lithological and thermobaric conditions within sedimentary successions, resulting in distinctive seismic characteristics that provide a means to distinguish the origin of cross-cutting reflectors (Somoza et al., 2014). In particular, silica diagenesis results in positive amplitude reflections, whereas GHs are associated with negative amplitude reflections (Bohrmann et al., 1992; Davies et al., 2002; Hein et al., 1978; Shipley et al., 1979).

Diagenesis in silica-rich sediments involves conversion of biogenetic

Opal-A to micro-crystalline Opal-CT at a transition zone known as $TZ_{A/CT}$ (Hesse, 1988; Wise Jr, 1972), which is usually tens of meters thick (Varkouhi et al., 2020). At greater depths, Opal-CT transforms to micro-crystalline Quartz known as Opaline Chert (e.g. Hesse, 1988; Kastner et al., 1977b; Wise Jr, 1972; Wrona et al., 2017). Silica transformation is a function of temperature (Grützner and Mienert, 1999; Kastner et al., 1977b), therefore the $TZ_{A/CT}$ extends (sub)parallel to the seafloor. Silica transformation across the $TZ_{A/CT}$ is accompanied by a noticeable decrease in porosity, permeability, and water content and an increase in density and P-wave velocity values (e.g. Guerin and Goldberg, 2002; Hesse, 1988; Isaacs, 1981; Meadows and Davies, 2010; Nobes et al., 1992). Therefore, the $TZ_{A/CT}$ appears as a BSR of positive polarity that cross-cuts the host strata, known as an Opal-A to Opal-CT BSR ($O_{A/CT}$_BSR) (Bohrmann et al., 1992; Davies and Cartwright, 2002; Hein et al., 1978). Since sediments beneath the $O_{A/CT}$_BSR contain Opal-CT, they show higher amplitude reflectors compared to those above (Berndt et al., 2004). $O_{A/CT}$_BSRs tend to lie at shallower sub-bottom depth with increasing water depth, due to favored diagenesis at higher pressures (Berndt et al., 2004).

Studies have shown that the $TZ_{A/CT}$ can also lie at an angle to the

present-day seafloor, defining non-bottom simulating reflectors (OA/CT_NBSR) (e.g. Brekke et al., 1999; Davies and Cartwright, 2002; Roaldset and Wei, 1997; Rundberg, 1989). The difference between an $O_{A/CT}$_BSR and an $O_{A/CT}$_NBSR is explained by the concept of fossilized silica diagenetic fronts. An 'active' $TZ_{A/CT}$, which corresponds to an $O_{A/CT}$_BSR on seismic profiles, is defined as one in equilibrium with present-day thermal regime within the sediment column (Neagu et al., 2010) and is conformable to the present isotherm. A 'fossilized' (or 'arrested') $TZ_{A/CT}$, which corresponds to an $O_{A/CT}$_NBSR on seismic profiles, on the contrary, formed under a palaeo-thermal regime other than that of the present-day and therefore appears inclined to the present seafloor bathymetry. It is hypothesized that a fossilized $TZ_{A/CT}$ is either a product of an abrupt change in temperature regime or a consequence of a major discontinuity in sediment accumulation (Meadows and Davies, 2010; Varkouhi et al., 2022). Table 1 summarizes the reviewed criteria (Varkouhi et al., 2022) to discern between active and fossilized $TZ_{A/CT}$.

Gas hydrates are clathrates of methane (or higher- and non-hydrocarbons) and water which form under low temperatures (<25 °C) and high pressures (>0.6 MP) (Kvenvolden, 1994; Sloan Jr, 1998). Sediments hosting GHs show increased P-wave velocity values due to increased rigidity of the sediment succession (e.g. Sloan Jr, 1998; Whalley, 1980). Below the base of the GH stability zone (BGHS), free gas and/or dissolved gas account for a drastic drop in P-wave velocity values (e.g. Domenico, 1977; Lee, 2004) and in seismic frequency content (Carcione and Picotti, 2006; Taner et al., 1979, 1994). Thus the BGHS appears as a negative polarity reflector on seismic profiles (Shipley et al., 1979). The depth-dependent thermobarometric conditions for the formation of GHs cause the BGHS to lie (sub)parallel to the seafloor on the seismic sections (GH-BSR) (Shipley et al., 1979), deepening slightly as water depth increases due to increased hydrostatic pressure and decreased water bottom temperature (Berndt et al., 2004).

Seismic diagnostic criteria have been used to identify diagenetic fronts and gas-hydrate intervals in basins worldwide (e.g. Berndt et al., 2004; Geletti and Busetti, 2011; Lodolo et al., 1993; Nouzé et al., 2009; Sain et al., 2000; Shedd et al., 2012). In turn, the cross-cutting reflections associated with these occurrences can also provide information on the evolutionary history and the paleoenvironmental conditions of the host sedimentary basin (e.g. Davies, 2005; Davies and Clark, 2006; Neagu et al., 2010; Nicholson and Stow, 2019). The geometrical, morphological, and depth characteristics of diagenetic – and gas-hydrate related reflectors provide a basis to learn about basin-wide (palaeo)thermal conditions (e.g. Kuramoto et al., 1992; Meadows and Davies, 2010; Minshull and Keddie, 2010; Ohde et al., 2018). Popescu et al. (2006) discussed the potential of using characteristics of BSRs on seismic data from the Black Sea as proxies for paleoclimatic conditions. Pérez et al. (2021) held a thicker-than-present sedimentary cover in Pennell Basin responsible for the silica diagenesis in the basin; they suggested that the overburden underwent extensive erosion and thinning due to recurrent ice advances in this basin.

Previous studies from the Falkland/Malvinas Plateau have noted the presence of cross-cutting reflectors that have been proposed to be of diagenetic origin (Cunningham, 1999; Koenitz et al., 2008). However, the characteristics of these reflectors have not been examined in detail, nor have they been considered in terms of fossil or active diagenetic processes during the thermal evolution of the basin. On the Falkland/-Malvinas Terrace, close to the Falkland/Malvinas Islands, Nicholson and Stow (2019) attributed the depth character of a diagenetic BSR to the erosive action of the core of the Sub Antarctic Front (SAF).

The aim of this study is to investigate the nature of cross-cutting reflectors across the Falkland/Malvinas Plateau through analysis of their seismic characteristics and with reference to lithological, thermal

Table 1
Summary of criteria used for discerning the status of a silica diagenetic front (active vs. fossilized), modified from Varkouhi et al. (2022). The colors indicate the degree of reliability attributed to each feature; red (low), yellow (intermediate), and green (high).

Criteria		Argument for Active diagenetic front	Argument for Fossilized diagenetic front	Reliability
Geometrical	1. a. $TZ_{A/CT}$ appears as a BSR	✔		(yellow)
	1. b. $TZ_{A/CT}$ appears as an NBSR	X	✔	(green)
	1. c. $TZ_{A/CT}$ terminates at the seafloor	X	✔	(green)
Structural	2. a. Regional anticlines/synclines above the $TZ_{A/CT}$		✔	(yellow)
	2. b. Differential compaction folding above the $TZ_{A/CT}$		✔	(red)
	2. c. Polygonal faulting in the vicinity of the $TZ_{A/CT}$		✔	(red)
Combination of 1.b., 2. a., 2. b., and 2. c.		X	✔	(green)

and velocity information available from Deep Sea Drilling Project (DSDP) Sites 327, 329, 330, and 511 (Fig. 1). We argue the seismic character of the cross-cutting reflectors to be consistent with fossiled diagenetic fronts, and examine their formation in relation to past changes that could account for their formation. Our findings have implications for the thermal, sedimentary and oceanographic evolution of this area of the South Atlantic.

2. Geological and oceanographic background

The Falkland/Malvinas Plateau is an elongated submarine plateau in the southwest South Atlantic, some 600 km east of the South American mainland. It comprises three distinct provinces, from west to east: the Falkland/Malvinas Islands (F/MI), the Falkland/Malvinas Basin (F/MB), and the Maurice Ewing Bank (MEB) (e.g., Lorenzo and Mutter, 1988; Shipboard Scientific Party, 1974a, c, b, 1980) (Fig. 1). The F/MB lies between the more elevated F/MI and MEB, with average water depths of 2600 m, and forms a 500 km-wide basin containing a sedimentary column up to ca. 3000 m thick above basement (Lorenzo and Mutter, 1988; Najjarifarizhendi and Uenzelmann-Neben, 2021; Richards et al., 1996).

The Falkland/Malvinas Plateau is confined to the north by the Falkland Escarpment, a basement ridge that is the result of strike-slip motion along transform faults (Ludwig, 1983), which gives way to the Falkland-Agulhas Fracture Zone (Ben Avraham et al., 1997; Lorenzo and Mutter, 1988; Ludwig, 1983) (Fig. 1). The west-east trending Falkland/Malvinas Trough (F/MT) is a 1000 km-long bathymetric depression formed by transform movement between the South American and Scotia plates (Fig. 1). The seabed in the F/MT deepens into the Georgia Basin in the east while it shoals westwards towards the South American continental shelf (Schreider et al., 2010). The F/MT extends 1300 km from the South American continental shelf where it lies at ca. 3250 m water depth with a width of less than 9 km at about 49°W, while eastwards it deepens to more than 3750 m and widens to ca. 50 km at 46°W, giving way to the Georgia Basin at ca. 41°W (Cunningham and Barker, 1996).

The sedimentary history of the F/MB has been inferred from DSDP drill sites in its easternmost sector (Fig. 1). Middle to late Jurassic sediments rest unconformably on granitic basement and characterize an open shelf environment, in which sapropelic claystone was deposited under euxinic conditions by Oxfordian times
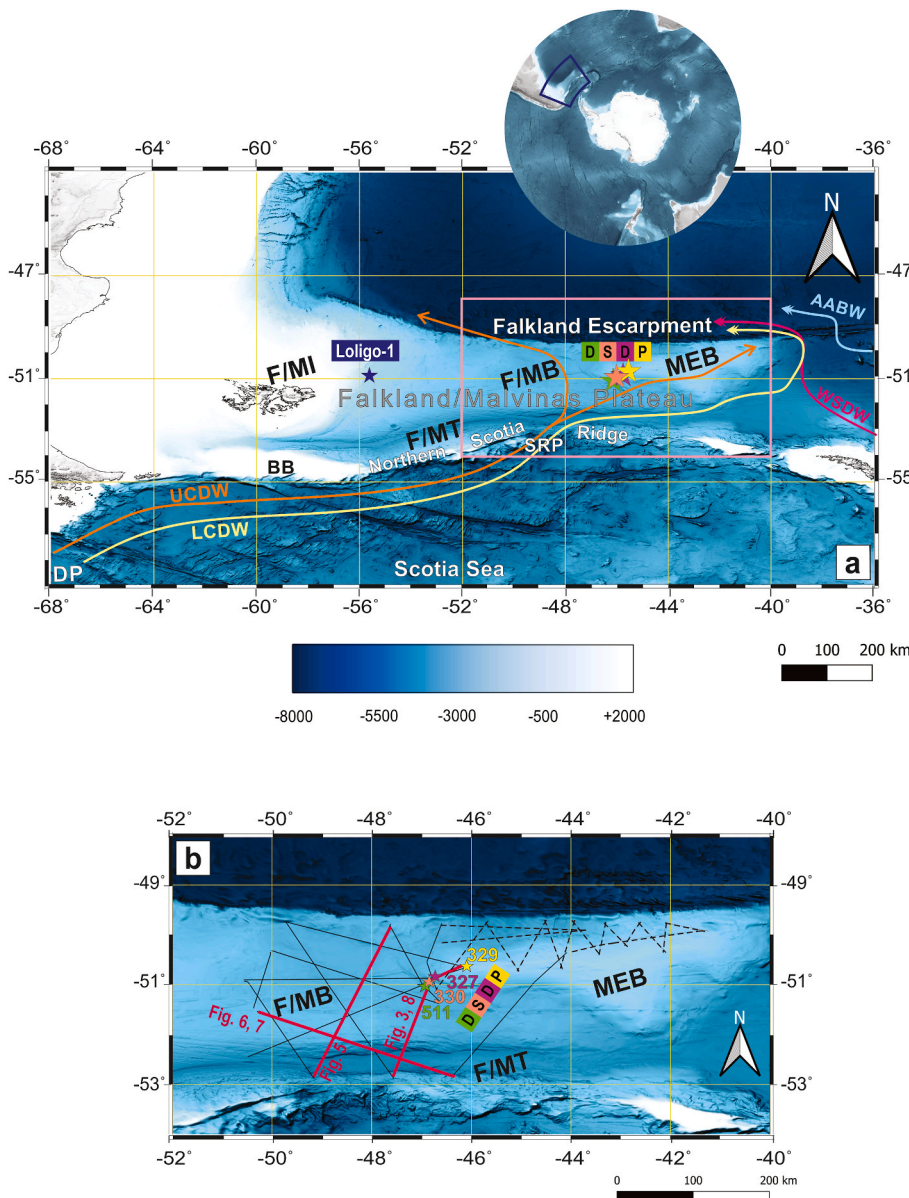

Fig. 1. (a) Bathymetric map showing the location of the Falkland/Malvinas Plateau in the Southern Ocean (General Bathymetric Chart of the Oceans (GEBCO_2022)). Arrows schematically show the pathways of the southern-sourced deep/bottom water masses in the present oceanic scheme (Arhan et al., 1999; Arhan et al., 2002; Orsi et al., 1999; Shipboard Scientific Party et al., 1980). Upper Circumpolar Deep Water (UCDW) in orange, Lower Circumpolar Deep Water (LCDW) in yellow, Weddell Sea Deep Water (WSDW) in pink, and Antarctic Bottomwater (AABW) in blue. BB=Burdwood Bank; DP = Drake Passage; F/MB = Falkland/Malvinas Basin; F/MI = Falkland/Malvinas Islands; F/MT = Falkland/Malvinas Trough; MEB = Maurice Ewing Bank; SRP=Shag Rocks Passage. Stars mark the location of DSDP Leg 36 Sites 327, 329, and 330 and Leg 71, Site 511 and the commercial borehole Loligo-1 in the study area. (b). Superimposed are the locations of the seismic profiles used for this study, shown as solid lines. Dark red lines illustrate the location of profiles shown in figures. Light dashed lines illustrate part of the dataset across the MEB, which have been the focus of the publication studied by Najjarifarizhendi and Uenzelmann-Neben (2021). Stars mark the locations of DSDP Leg 36 Sites 327, 329, and 330 and Leg 71, Site 511. (For interpretation of the references to color in this figure legend, the reader is referred to the Web version of this article.)

(Shipboard_Scientific_Party, 1977). A combination of rapid subsidence and early connections between the Indian and Proto-Atlantic oceans led to open marine conditions by the Albian (e.g. Barker, 1977; Dummann et al., 2020; Ludwig, 1983; Shipboard_Scientific_Party, 1974a, 1974c, 1980). A Cretaceous-Tertiary unconformity that spans 25 My has been associated with a carbonate-poor ocean, as well as oceanographic changes in the Southern Ocean (e.g. Barker, 1977; Ciesielski and Wise Jr, 1977; Dummann et al., 2020; Ludwig, 1983; Shipboard_Scientific_Party, 1974a, c, 1980). The Paleogene and Neogene sequences include erosional and/or non-depositional unconformities that record major hiatuses (for details see Fig. 2 in Najjarifarizhendi and Uenzelmann-Neben (2021)). The two most prominent unconformities, the Eocene-Oligocene and Middle-Late Miocene, have been linked to the onset of a proto-Antarctic Circumpolar Current (ACC) and intensified deep and bottom water production consequent to the perennial glaciations of Antarctica (e.g. Barker, 1977; Barker and Thomas, 2004; Scher and Martin, 2006a; Shipboard_Scientific_Party, 1974a, b, c, 1980).

In the oceanographic setting of the Southern Ocean, the southwest South Atlantic forms an important gateway for interoceanic exchanges of mass and energy. The Falkland/Malvinas Plateau lies in the pathway of the ACC (Fig. 1a) and accommodates the transfer of a total of ~100 Sv of deep and bottom water masses (Arhan et al., 2002; Orsi et al., 1995). The water masses in the area are of different origins and comprise Weddell Sea Deep Water (WSDW), Antarctic Bottom Water (AABW), Lower Circumpolar Deep Water (LCDW), and Upper Circumpolar Deep Water (UCDW) (Arhan et al., 1999, 2002; Orsi et al., 1999) (Fig. 1). Downstream of the Drake passage, at about 66°W, the major part of the ACC transport is diverted northward by the SAF and Polar Front (PF), which then form a western and an eastern branch after skirting the Burwood Bank (Fetter and Matano, 2008). The F/MB takes in the western branch on its way towards the Argentine Basin, while the eastern branch flows along the PF and rounds the MEB before merging with the western branch at 48°W to form the Falkland/Malvinas Current (Fig. 1a).
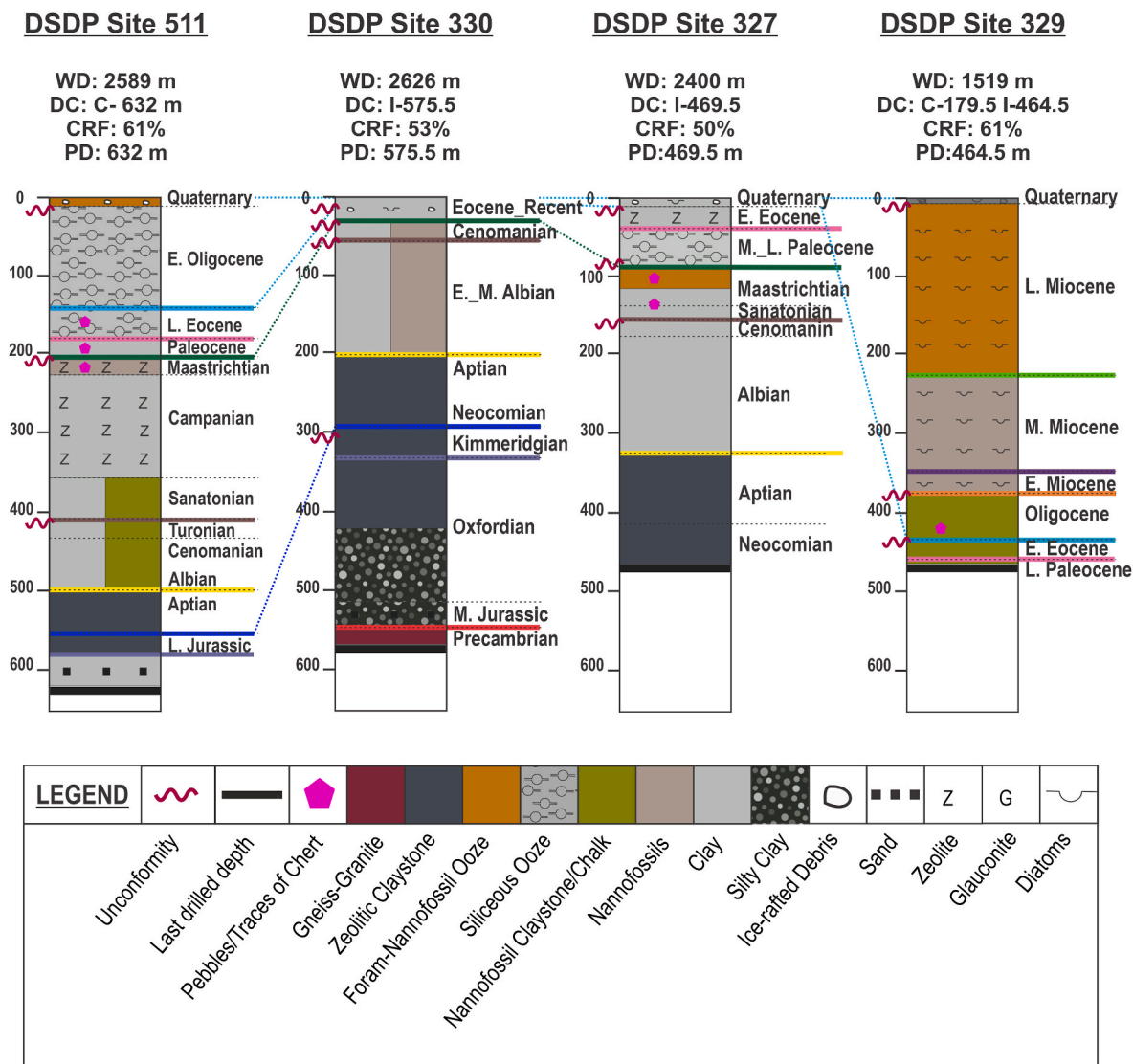

Fig. 2. Summary of results from DSDP Leg 36 Sites 327, 329, and 330 and Leg 71, Site 511 (Shipboard_Scientific_Party, 1974a, 1974b, 1974c; 1980). Schematically shown for each site are the reported lithological information, hiatuses, and geological ages plotted against depth below seafloor. WD, DC (C or I), PD, and CRF values stated for each site respectively represent Water Depth, Drilled Core (Continuously Cored or Intermittently Cored), penetration depth, and Core Recovery Factor. The marker horizons defined in the seismostratigraphic model are also color marked (for details, see Fig. 4 and Section 3.3, and Appendix B). (For interpretation of the references to color in this figure legend, the reader is referred to the Web version of this article.)

3. Data and methods

3.1. Seismic reflection data

This study uses a subset (ca. 3300 km) of 2D seismic reflection data from the 2019 RV *Maria S. Merian* cruise MSM81 (Uenzelmann-Neben, 2019), covering the central and the eastern sections of the F/MB and F/MT (solid lines in Fig. 1b). The seismic source comprised an array of 4 GI-guns with a total volume of ca. 9.6 l and was fired every 25 m, producing signals with frequencies of up to 300 Hz and a dominant frequency of 80 Hz. For a reflector at depth of ca. 3000 m with an average velocity of 2500 m/s, considering signal frequency of 80 Hz, this implies $\cong$ 10 m vertical resolution. Each individual GI-gun consisted of a generator chamber (0.72 l volume) and an injector chamber (1.68 l volume), the latter triggered with a 33 ms delay to minimize the bubble effect. The data were acquired using a 240-channel digital seismic streamer (SERCEL SEAL©) with a hydrophone array spacing of 12.5 m (total active length 3 km) and a 141.4 m-long lead-in cable. Data were recorded at a 1 ms sampling rate over a record length of 9 s.

Pre-processing of the seismic data included navigation merge, geometry definition, and CDP-sorting with a 25 m CDP spacing. Normal-move-out corrections were applied based on a precise velocity analysis (at least every 50 CDPs or ∼1.25 km), using RMS velocity values in semblance method. Semblance velocity attribute as a means of RMS velocity analysis sweeps CDP gathers for a range of velocities along the time axis; where for matching velocities with reflectors, semblance attribute gives higher correlation values (Yilmaz, 2001). Amplitude attenuation due to geometric spreading was accounted for in producing the stacked data. In order to reconstruct a true subsurface image, especially in areas with high reflector inclinations, an Omega-X post-stack time migration step (Yilmaz, 2001) was applied. In order to preserve amplitudes, no Automatic Gain Control filter (AGC) was used in the processing sequences or for display. Displayed sections include a bandpass filter with a Hanning Window taper with low and high boundaries of 5–30 Hz and 200–250 Hz, respectively. Appendix A summarizes the seismic data processing workflow.

Seismic attributes were derived from the original seismic data using mathematical methods. These quantify the changes in characteristics of seismic waves, such as amplitude, frequency, phase, velocity, as they propagate through the earth layers and are subjected to varying physical properties (Aminzadeh and Dasgupta, 2013). Trace attributes are considered as convenient display forms; however, they can also be used as analytic geophysical tools that provide information on lithological properties (Taner, 2001). In this study we use three post-stack geometrical attributes. Instantaneous frequency is the time derivative of the phase, which responds both to wave propagation effects as well as depositional characteristics. It is known as an indicator of lower frequency zones such as fracture zones or gas accumulations (Subrahmanyam and Rao, 2008). The first envelope derivative shows the variation of the energy of reflected events and is a good discriminator of absorption effects (Subrahmanyam and Rao, 2008). Energy attribute is a measure of reflectivity in specified time windows, which is useful for amplitude anomaly detection. Meaning higher energy correlates with higher reflectivity (Johnston, 2010).

3.2. Drilling data and age model

DSDP Legs 36 and 71 drilled four Sites 327, 329, 330, and 511 in the westernmost MEB (Fig. 1b). Results from each site, including water depth, total drilled and cored depths, total core recovery, and lithological information are summarized in Fig. 2 (Shipboard_Scientific_Party, 1974a, b, c; 1980). No downhole geophysical logs were acquired at the four DSDP sites, but velocity measurements on cored sections yielded interval velocities which we used to convert from the depth to time domains (Najjarifarizhendi and Uenzelmann-Neben, 2021). The velocity data were used to correlate information from the drill sites with seismic

profiles in order to construct an age-constrained stratigraphic model for the eastern part of the Falkland/Malvinas Plateau (see Appendix B).

4. Results

4.1. Stratigraphic context

Seismic reflection profiles correlated to drilling data show the study area to consist of Precambrian basement overlain by a sedimentary succession up to 3 km thick, that records deposition since the Middle-Late Jurassic (Figs. 3, 4) (Najjarifarizhendi and Uenzelmann-Neben, 2021). Previous work by Najjarifarizhendi and Uenzelmann-Neben (2021) on the MEB, has divided the succession into five main units, shown in Fig. 3 on a composite profile crossing the DSDP sites. The stratigraphic model is detailed in Appendix B, including modifications adopted in this study in extending it towards the F/MB and F/MT. Unit SU3 has been modified to SU3' to represent Late Cretaceous strata within the F/MB, which unlike the MEB includes thick packages sub-divided into five subunits separated by four unconformities. Furthermore, the distinct mounded morphology of Post-Oligocene strata within the F/MT, which is dissimilar with strata of the same age elsewhere on the Falkland/Malvinas Plateau, called for introducing Unit 6 (Fig. 4).

4.2. Cross-cutting reflectors

4.2.1. Reflector XR-F/MB

In the F/MB, a very high amplitude, continuous to discontinuous reflector extends (sub)parallel to the seafloor (reflector R–SF) and cross-cuts reflectors of (sub)units SU3'-e, SU4 and SU5 (Fig. 3, AWI-20190004, CDPs 2500–5000, Fig. 5a, CDPs 2000–5000, and Fig. 6, CDPs 600–8000). The reflector is identified on seismic profiles southwards from ca. 50°S in the F/MB and in places can be traced onto the northern flank of the F/MT. Reflector XR-F/MB is mostly recognized within the western and central parts of the F/MB, whereas towards the east it becomes difficult to trace (Figs. 3 and 5a). Reflector XR-F/MB has the same polarity as seafloor reflector R–SF (Fig. 5b) and appears as a high-energy interface using the seismic attribute energy, which is proportional to the reflection coefficient of the reflecting interface (Fig. 5d). Reflector XR-F/MB lies 500–550 ms TWT below seafloor (msTWTbsf) and shoals slightly towards the south with increasing water depth (Fig. 6a). Reflector XR-F/MB in places shows serrated reflection patterns (Fig. 6b), including asymmetrical saw-tooth morphologies with heights ranging from 20 to 60 ms TWT.

4.2.2. Reflector XR-F/MT

Reflector XR-F/MB can in places be traced onto the northern flank of the F/MT, where it gives way to a continuous and very high amplitude reflector (hereafter called reflector XR-F/MT) that cross-cuts the host strata of subunit SU6-a within the F/MT (Fig. 3, AWI-20190004, CDPs 1200–2400 and Fig. 6, CDPs 8600–10600). Reflector XR-F/MT has high reflectivity (Fig. 5d) and the same polarity as the seafloor reflector R–SF (Fig. 5c). Reflector XR-F/MT is not parallel to the seafloor reflector in the F/MT; instead, it seems to replicate the geometry of reflector R-EMM (Fig. 3, AWI-20190004, CDPs 1000–2500 and Fig. 6, CDPs 8600–10600). This reflector is identified between ca. 46–49°W across the F/MT.

4.3. Distinctive features associated with cross-cutting reflectors

In the presence of reflector XR-F/MB, adjacent strata, including (sub) units SU3'-e, SU4 and SU5, in places are highly affected by faulting (Fig. 6b). Numerous small-scale faults with average throws of about 40 ms TWT have deformed the strata surrounding reflector XR-F/MB, where partially serrated reflection patterns are formed (Fig. 6b). The fault displacements decrease throughout subunits SU3'-a to SU3'-d and most do not propagate into underlying strata (compare the strata below
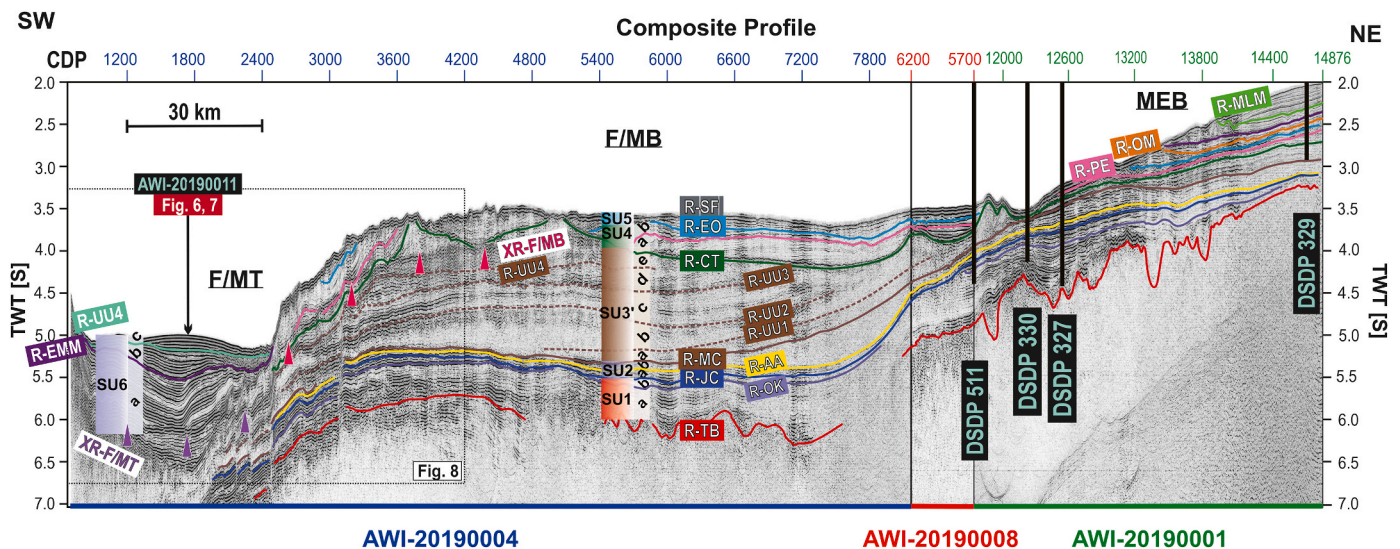
Fig. 3. Interpreted composite seismic profile (from profiles AWI-20190001, AWI-20190008, AWI-20190004). Location of profile is shown in Fig. 1b. Superimposed are the marker horizons defined in the seismostratigraphic model (for details, see Fig. 4, Section 3.3, and Appendix B). The location of the DSDP Sites 327, 329, and 330 and Leg 71, Site 511 crossed by the seismic lines are marked with thick black lines. The pink and purple triangles respectively mark the cross-cutting reflectors XR-F/MB and XR-F/MT (for details, see Section 4.1). The black box marks the zoomed section shown in Fig. 8. Arrow shows the location of crossing seismic profile. (For interpretation of the references to color in this figure legend, the reader is referred to the Web version of this article.)

and above reflector XR-F/MB in Fig. 6b, CDPs 6000–6800). In comparison, reflector XR-F/MT is less affected by fault sets, yet the faults have similar characteristics to those in the F/MB (Fig. 6c, CDPs 8600–10000). These faults show small throws, no systematic orientation, and mainly deform strata above reflector XR-F/MT including subunits SU6-a and SU6-b.

Considering reflectors from the same stratal units, successions below the cross-cutting reflector XR-F/MB show higher amplitudes than those above (Fig. 6b). Above reflector SR-F/MB, internal reflectors of (sub) units SU3′-e, SU4, and SU5 locally show irregular deformation features as product of faulting (Fig. 6b). These include a series of anti- and synclinal folds, with an average wavelength of ca. 1250 m, that are not characteristic of these units elsewhere on the F/MB.

Seismic attributes provide information on the cross-cutting reflectors (Figs. 7, 8). Reflectors XR-F/MB and XR-F/MT both appear as high-velocity reflections on semblance attribute sections, which provide a measure of the RMS velocity values (Fig. 7b and c). Across both reflectors, an average velocity increase of about 75 m/s is observed on semblance profiles. Interval velocity sections also indicate a noticeable increase across these two reflectors (Fig. 7a).

Instantaneous frequency attribute sections show no significant change across reflectors XR-F/MB and XR-F/MT, indicating that they are not associated with strong changes in frequency content (Fig. 8a). The low absorption effect of reflectors XR-F/MB and XR-F/MT is also inferred from the seismic attribute first envelope derivative, which indicates little change in energy across the reflecting interfaces (Fig. 8b).

5. Discussion

The cross-cutting character of reflectors XR-F/MB and XR-F/MT (Figs. 3, 5a and 6a) clearly indicate them to be products of post-depositional processes. Below, we present arguments for their origin as fossilized silica diagenetic fronts and their palaeoceanographic implications.

5.1. Diagenetic origin of cross-cutting reflectors

DSDP Sites 327 and 511 documented the prevalence of siliceous ooze in the post-Tertiary sediments and traces of chert in Late Cretaceous sediments (Ciesielski and Wise Jr, 1977; Shipboard_Scientific_Party,

1974a, c, 1980) (Fig. 2). Piston and Kasten cores also provide evidence for Neogene silica-rich sediments across the F/MT (Allen et al., 2011; Allen et al., 2005; Cunningham, 1999; Rivas et al., 2018; Saito et al., 1974). From a lithological perspective, this supports the diagenetic nature of reflectors XR-F/MB and XR-F/MT, since silica diagenesis can only take place in presence of silica-rich sediments (Berndt et al., 2004).

The two cross-cutting reflectors have the same positive (normal) polarities as the seafloor reflector (Fig. 5b and c). This observation rules out their origin as GH-BSRs, which are associated with negative (reversed) polarities due to the presence of gas beneath the BGHS. The very high positive amplitudes of reflectors XR-F/MB and XR-F/MT (Figs. 3, 5a and 6a) are instead consistent with the expected characteristics of a $TZ_{A/CT}$, for which silica diagenesis causes porosity and water content to drop considerably, leading to decreased acoustic impedance (Bohrmann et al., 1992; Davies and Cartwright, 2002; Hein et al., 1978).

In general, reflections from the same seismic event show an increase in amplitude below reflector XR-F/MB (Fig. 6b). This observation could be due to the presence of Opal-CT below the $TZ_{A/CT}$, which leads to higher acoustic impedance and thus to stronger reflectivity (Berndt et al., 2004; Bohrmann et al., 1992; Davies and Cartwright, 2002; Hein et al., 1978). The serrated character of the cross-cutting reflector observed in some places is considered to be due to variations in Opal-A content of the overlying strata which result in preferential upward advancement of $TZ_{A/CT}$ in zones with Opal-A-rich content (Varkouhi et al., 2022).

Semblance profiles and interval velocity sections (Fig. 7) indicate a noticeable velocity increase below reflectors XR-F/MB and XR-F/MT, typical of diagenetic fronts (e.g. Guerin and Goldberg, 2002; Hesse, 1988; Isaacs, 1981; Meadows and Davies, 2010; Nobes et al., 1992). Moreover, no significant lateral variations in interval velocities are observed within the top 1500 ms TWT below the seafloor, inclusive of units SU4 and SU5 and reflector XR-F/MB (Fig. 7a). Hence, the observation that reflector XR-F/MB shoals in greater water depth on the seismic profiles (Fig. 6) is not velocity dependent and can be attributed to the actual subsurface geometry. This phenomenon has been explained for $TZ_{A/CT}$ by the higher effective pressure of the water column as the water depth increases (Berndt et al., 2004).

The instantaneous frequency attribute has been used to identify free-gas zones, for example below the BGHS (e.g.Geletti and Busetti, 2011; Kim et al., 2013; Taylor et al., 2000; Vanneste et al., 2002). No drastic
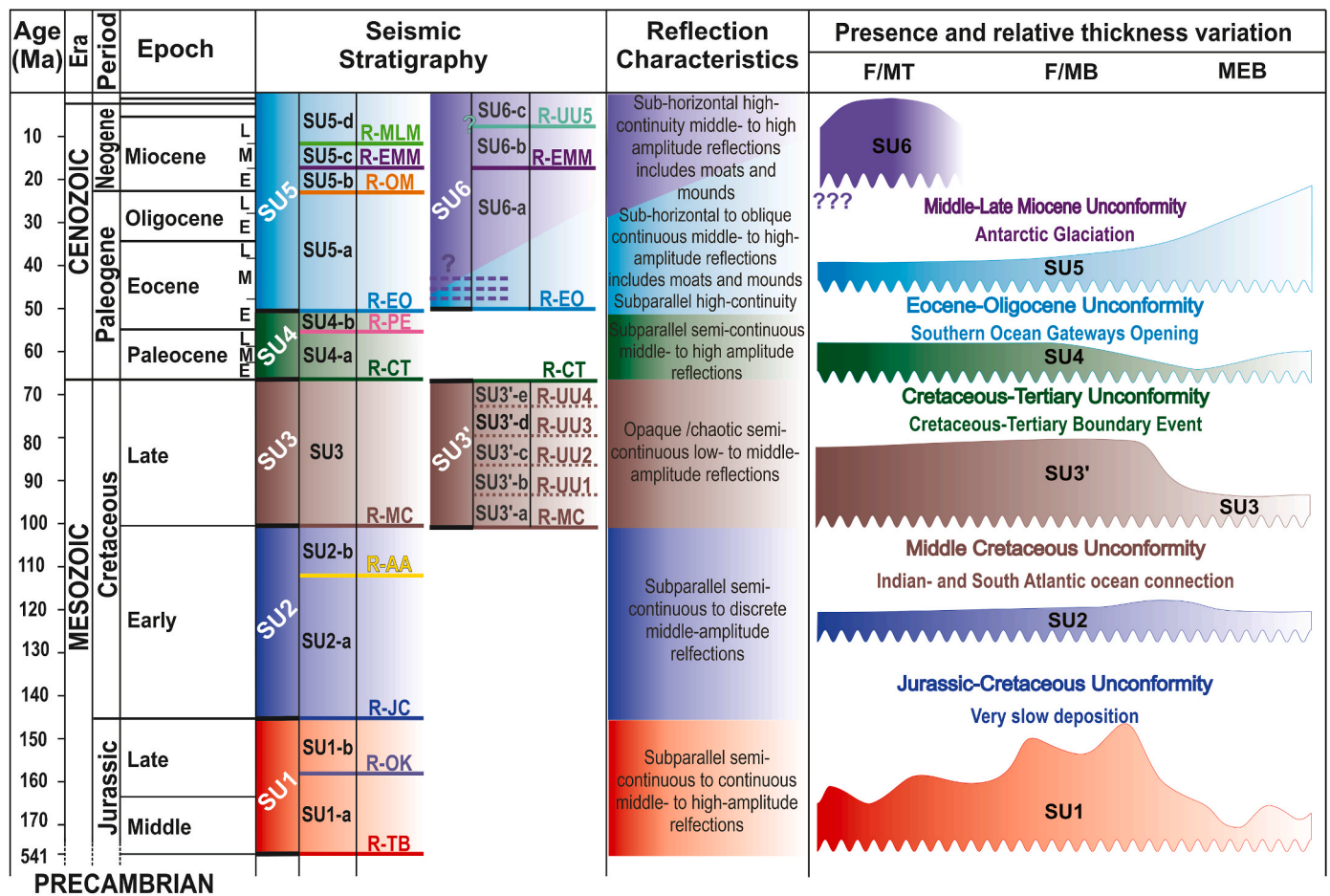
Fig. 4. Summary of the seismostratigraphic model for the Falklands/Malvinas Plateau, showing units and marker horizons (at left), generalized reflection characteristics (middle column) and relative thickness variations (right-hand column). Left column is the seismostratigraphic model and seismic units across the Falkland/Malvinas Plateau. The marker horizons and seismic units for the eastern sector of the Falkland/Malvinas Plateau, after Fig. 2 in Najjarifarizhendi and Uenzelmann-Neben (2021) have been modified to include the new seismic unit SU3′ in the F/MB (for more details, see Fig. 5, Section 3.3. and Appendix B.2.2) and the new seismic unit SU6 in the F/MT (for details, see Figs. 3 and 5 and Section 3.3. and Appendix B.2.2). Unit SU3′ is introduced to represent Late Cretaceous strata in the F/MB, which unlike its coeval strata on the MEB (SU3), comprises 5 distinct subunits. Unit SU6, has been introduced to include the strata of post-Oligocene with a unique mounded morphology, restricted to F/MT, and differentiable from underlying unit SU5 elsewhere on the Falkland/Malvinas Plateau.

drop in frequency content is observed below reflectors XR-F/MB and XR-F/MT, as expected for a GH-BSR (Fig. 8). The seismic attribute first envelope derivative displays rapid changes across reflectors XR-F/MB and XR-F/MT indicating a wide bandwidth and weak absorption effects (Fig. 8b). Seismic units SU4 and SU5 are extremely affected by small-scale fault sets (throw values ≈ 40 ms TWT), especially where reflectors XR-F/MB and XR-F/MT are present (Figs. 5d, 6b and 6c). Since these faults do not show a particular orientation and are layer-bound (confined to specific stratigraphic units) without any indication for a deeper tectonic origin, we categorize these as polygonal faults associated with the abrupt compaction across the $TZ_{A/CT}$ (Bünz et al., 2003; Davies et al., 2009; Nouzé et al., 2009; Volpi et al., 2004). Folds, observed above reflectors XR-F/MB and XR-F/MT within seismic units SU4 (Fig. 6b), are interpreted as features of differential compaction, as observed in other areas associated with silica transformation (Davies, 2005; Neagu et al., 2010; Varkouhi et al., 2022).

5.2. Cross-cutting reflectors as fossilized silica diagenetic fronts

Reflector XR-F/MB is a BSR observed at a constant depth of 500–550 msTWTbsf, while reflector XR-F/MT is an NBSR that varies in depth relative to the seafloor (Fig. 6a). A BSR does not necessarily indicate an active diagenetic front (Varkouhi et al., 2022), while an NBSR clearly points to the presence of a fossilized diagenetic front (Table 1) and

allows interpretation of reflector XR-F/MT as a fossilized $TZ_{A/CT}$. The structural peculiarities associated with reflector XR-F/MB, including polygonal faults and differential compaction folds (Fig. 6b), also argue in favor of its fossilized nature.

Fossilized diagenetic fronts in disequilibrium with present-day isotherms have been hypothesized to be the products of rapid changes in the regional thermal regime, or of long-lasting erosional phases within sedimentary basins (Meadows and Davies, 2010; Varkouhi et al., 2022). The fossilization time can be estimated from identification of the shallowest horizon with the same geometry as reflector XR-F/MT, which would have been the seafloor at the time of fossilization (arrest of the diagenetic front). This approach has been applied in several studies to estimate the time when upward migration of the $TZ_{A/CT}$ ceased (Davies and Cartwright, 2002; Meadows and Davies, 2010; Neagu et al., 2010). The seafloor in the F/MB, which we interpret to be an erosional surface, is formed by a Middle-Late Miocene reflector that dips southwards below younger strata in the F/MT (Figs. 3 and 6a). Piston and gravity sampling in the F/MB retrieved sediments of Oligocene-Miocene ages at seafloor (Saito et al., 1974).

The study of the processes which could contribute to the development of fossilized diagenetic fronts is still in its infancy, but such features are recognized to represent regional palaeo-isotherms (Meadows and Davies, 2010). Both reflectors XR-F/MB and XR-F/MT show good correspondence with the geometry of reflectors dated as Middle/Late
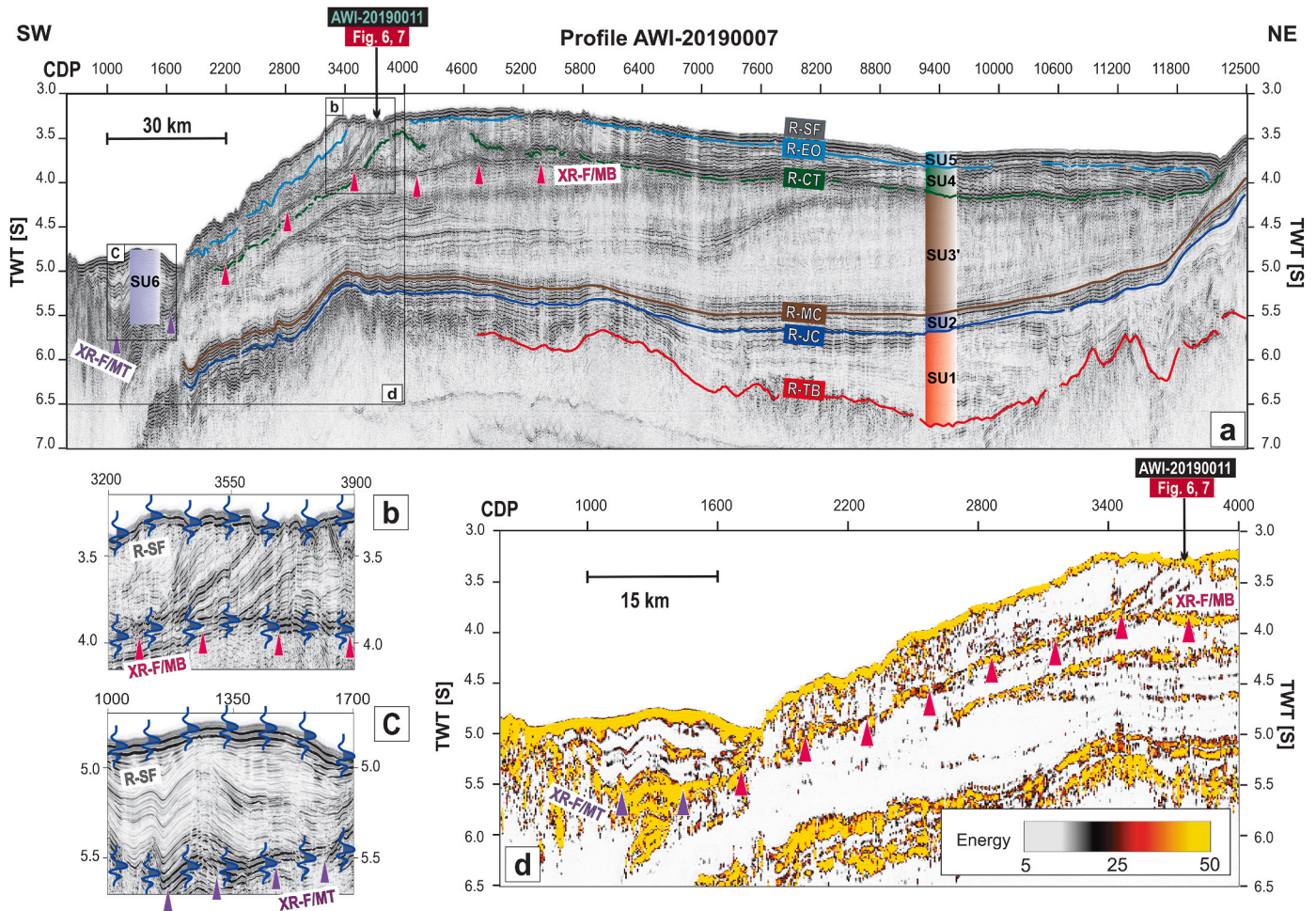
Fig. 5. (a) Interpreted seismic profile AWI-20190007. Location of profile is shown in Fig. 1b. Superimposed is the defined seismic stratigraphy and the marker horizons (for details, see Fig. 4, Sections 3.3 and Appendix B). The pink and purple triangles respectively mark the cross-cutting reflectors XR-F/MB and XR-F/MT (for details, see Section 4.1). Black boxes mark the zoomed sections shown in (b), (c), and (d). Arrow shows the location of crossing seismic profile. (b) and (c) Zoomed sections respectively showing the cross-cutting reflectors XR-F/MB and XR-F/MT; schematically shown are the polarity of the cross-cutting reflector compared to the seafloor reflector, typical of a positive polarity (for details, see Sections 4.1 and 6.1). (d) Zoomed section showing the seismic attribute "energy" (for details, see Section 4.1). Arrows show the location of crossing seismic profile. (For interpretation of the references to color in this figure legend, the reader is referred to the Web version of this article.)

Miocene (R–SF in F/MB and R-EMM in F/MT), suggesting this surface to correspond to the palaeo-isotherm that resulted in the formation of the fossilized $TZ_{A/CT}$ across the F/MB and F/MT (Figs. 3 and 6a).

5.3. Implications for regional palaeoceanographic evolution

The process of Opal-A/CT conversion is primarily controlled by temperature (e.g. Hein et al., 1978; Kastner et al., 1977a; Nobes et al., 1992; Varkouhi et al., 2020). In sedimentary basins where observed $O_{A/CT}$_BSRs were validated by borehole data, the reported temperatures for the Opal-A/CT conversion exceeded 35 °C (Berndt et al., 2004; Kuramoto et al., 1992; Neagu et al., 2010). Based on a study of progressive siliceous ooze diagenesis at Leg 19 DSDP sites, Hein et al. (1978) also found that temperatures exceeding 35 °C, effective at least for 10 My, were required for Opal-A/CT conversion in shallow marine sediments.

Geothermal gradients are available from temperature measurements in two boreholes within the study area. DSDP Site 511 in the easternmost sector of the F/MB yielded a value of 74 °C/km (Langseth and Ludwig, 1983), and commercial borehole Loligo-1 in the westernmost sector of the Falkland/Malvinas Plateau reported 38.5 °C/km (Nicholson and Stow, 2019) (Fig. 1). In addition, based on analysis of a gas

hydrate BSR in the Malvinas Basin, Baristeas et al. (2012) estimated a value of 23.9 ± 2.0 °C/km, southwest of the F/MI. These values yield an average thermal gradient of 45 °C/km. Seafloor temperature measurements at the locations of DSDP Site 511 (Langseth and Ludwig, 1983) and Loligo-1 (Nicholson and Stow, 2019), respectively, were 0.7 and 2 °C. These are in good agreement with oceanographic data from the F/MB, which indicate bottom water temperatures below 1.8 °C for the F/MB at water depths >2000 m, where influenced by LCDW (Arhan et al., 2002).

The temperature T (°C) at depth z (meters below seafloor (mbsf)) for a supposed temperature gradient $\frac{dT}{dz}$ (°C/km) and seafloor temperature T_{SF} (°C) is given by $T(z) = \frac{dT}{dz} * \frac{z}{1000} + T_{SF}$. The depth z (mbsf) of an observed reflector on the seismic section can be estimated by means of P-wave velocity v (m/s) and Two-way travel-time (msTWTbsf), given by z = vt/2. Reflector XR-F/MB lies on average 550 msTWTbsf (Fig. 6a), and interval velocities average 1900 m/s for the shallow marine sediments in the F/MB (Fig. 7). Using an average thermal gradient of 45 °C/km and seafloor temperature of 1 °C for the F/MB, the estimated temperature at the $TZ_{A/CT}$ equals 22.3 °C. Taking 35 °C as the minimum required temperature for onset of Opal-A/CT conversion (Berndt et al., 2004; Hein et al., 1978; Kuramoto et al., 1992; Neagu et al., 2010), the calculated temperature at the present depth of $TZ_{A/CT}$ in the F/MB
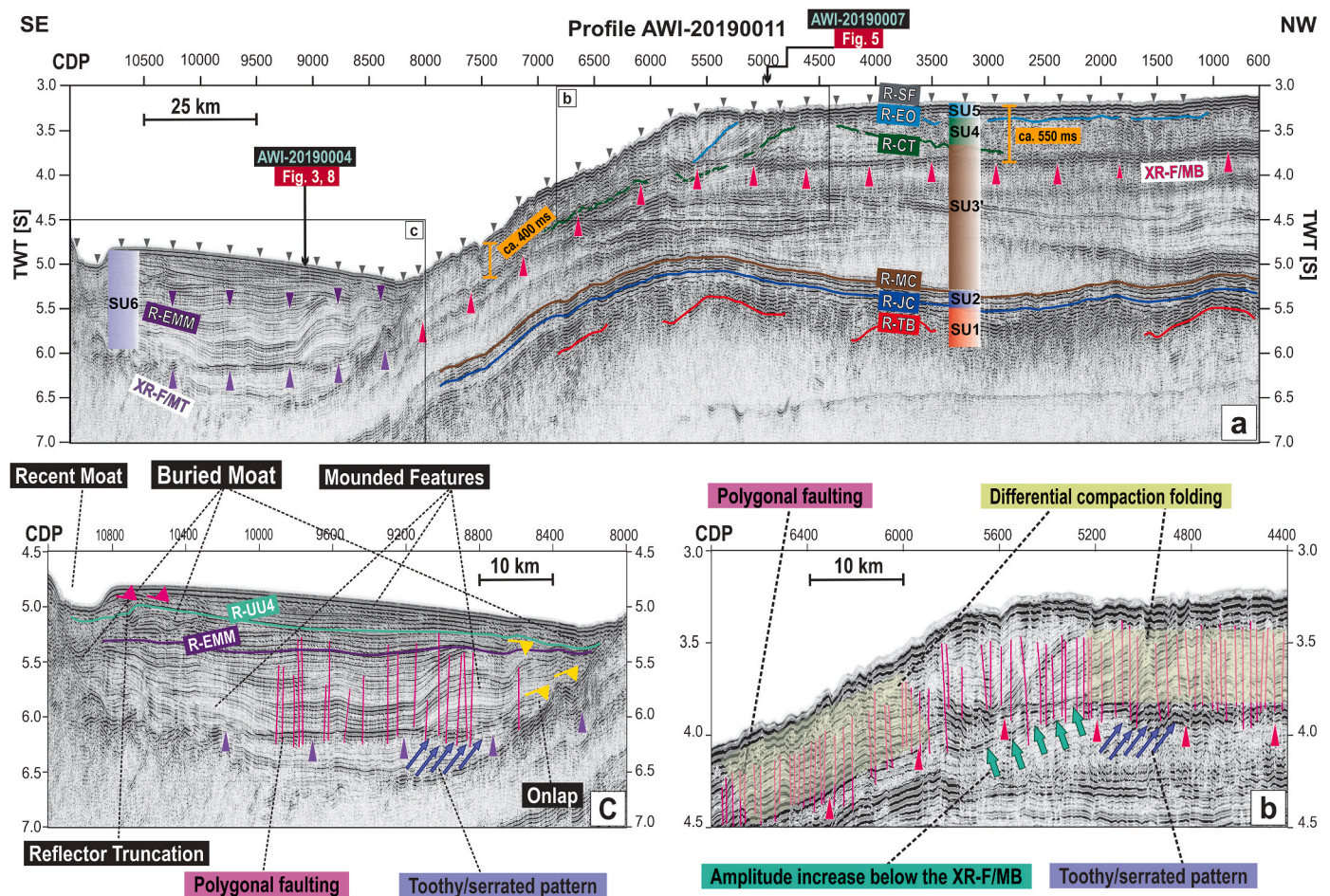
Fig. 6. (a) Interpreted seismic profile AWI-20190011. Location of profile is shown in Fig. 1b. Superimposed is the defined seismic stratigraphy and the marker horizons (for details, see Fig. 4, Sections 3.3 and Appendix B). The gray and violet triangles respectively mark the seafloor reflector (R–SF) and the Early-Middle Miocene unconformity (R-EMM) The pink and purple triangles respectively mark the cross-cutting reflectors XR-F/MB and XR-F/MT (for details, see Section 4.1). The black boxes mark the zoomed sections shown in (b) and (c). Arrows show the location of crossing seismic profiles. (b) and (c) Zoomed sections respectively showing the peculiar structural features in proximity of the cross-cutting reflectors XR-F/MB and XR-F/MT (for details, see Section6.2). (For interpretation of the references to color in this figure legend, the reader is referred to the Web version of this article.)

cannot account for this transition.

One possible explanation for the cessation of upward movement of the TZ$_{A/CT}$ in the F/MB is a rapid temperature drop at the seafloor in response to the onset of the ACC, when southern-sourced cold water masses reached the plateau at about the Eocene-Oligocene boundary (e. g. Barker, 1977; Najjarifarizhendi and Uenzelmann-Neben, 2021; Scher and Martin, 2006a; Scher and Martin, 2006b; Uenzelmann-Neben et al., 2017). Benthic foraminiferal proxy records at DSDP Site 511 suggest a temperature drop from 8 to 12.5 °C in the Eocene to ca. 2 °C in Oligocene times (Muza et al., 1980). Although a 10 °C temperature variation at the seafloor is significant, it cannot account for the thermal conditions required for the Opal-A/CT conversion in the F/MB. This implies a temperature of 32.3 °C at depth of reflector XR-F/MB, which is below the minimum temperature 35 °C suggested in the literature (Berndt et al., 2004; Hein et al., 1978; Kuramoto et al., 1992; Neagu et al., 2010) for the initiation of silica diagenesis.

A past regime of higher geothermal gradients could account for the present depth of the arrested silica diagenetic front across the F/MB. However, the present-day geothermal gradient measured at DSDP 511 (74 °C/km) is already higher than those reported in neighboring areas, such as Malvinas Basin (23.9 ± 2.0 °C/km) (Baristeas et al., 2012) and westernmost sector of the Falkland/Malvinas Plateau (38.5 °C/km) (Nicholson and Stow, 2019). Another means to account for the arrest of the silica diagenetic front is the removal of overburden, the presence of

which would have implied higher temperatures at depth. Taking 45 °C/km as the thermal gradient in the F/MB, an excess of ca. 270 m overburden would account for the minimum thermal requirement for Opal-A/CT conversion. This explanation is supported by analysis of the organic carbon content in sediments of Jurassic to Recent age at DSDP Site 511, which indicate an unusually high rate of maturation vs. burial depth (Dick et al., 1983). These authors relate this to either higher palaeo-thermal gradients of up to 100 °C/km or the removal of up to 400 m of overburden above the Cretaceous-Tertiary unconformity, or a combination of both. From seafloor exposures of Mesozoic sediments containing traces of well-lithified chert, Ciesielski and Wise Jr (1977) inferred erosion of a minimum of 150–200 m of sediments on the shoulder of the MEB near DSDP 330 (Fig. 3, AWI-20190001, CDPs 12100-12400).

The major erosional and non-depositional unconformities within the post-Tertiary sections at DSDP Sites 327, 329, 330, and 511 on the Falkland/Malvinas Plateau have been linked to the influx of deep and bottom water masses subsequent to the opening of the Drake Passage (Barker, 1977; Ciesielski and Wise Jr, 1977; Shipboard_Scientific_Party, 1974a, 1974c, 1980). The most extensive erosional phase has been attributed to the Late Miocene, with intensified deep and bottom water formation in response to the growth of ice sheets in Antarctica (Shipboard_Scientific_Party, 1974a, b). The absence of sedimentary strata younger than the Miocene in drill core data in the F/MB
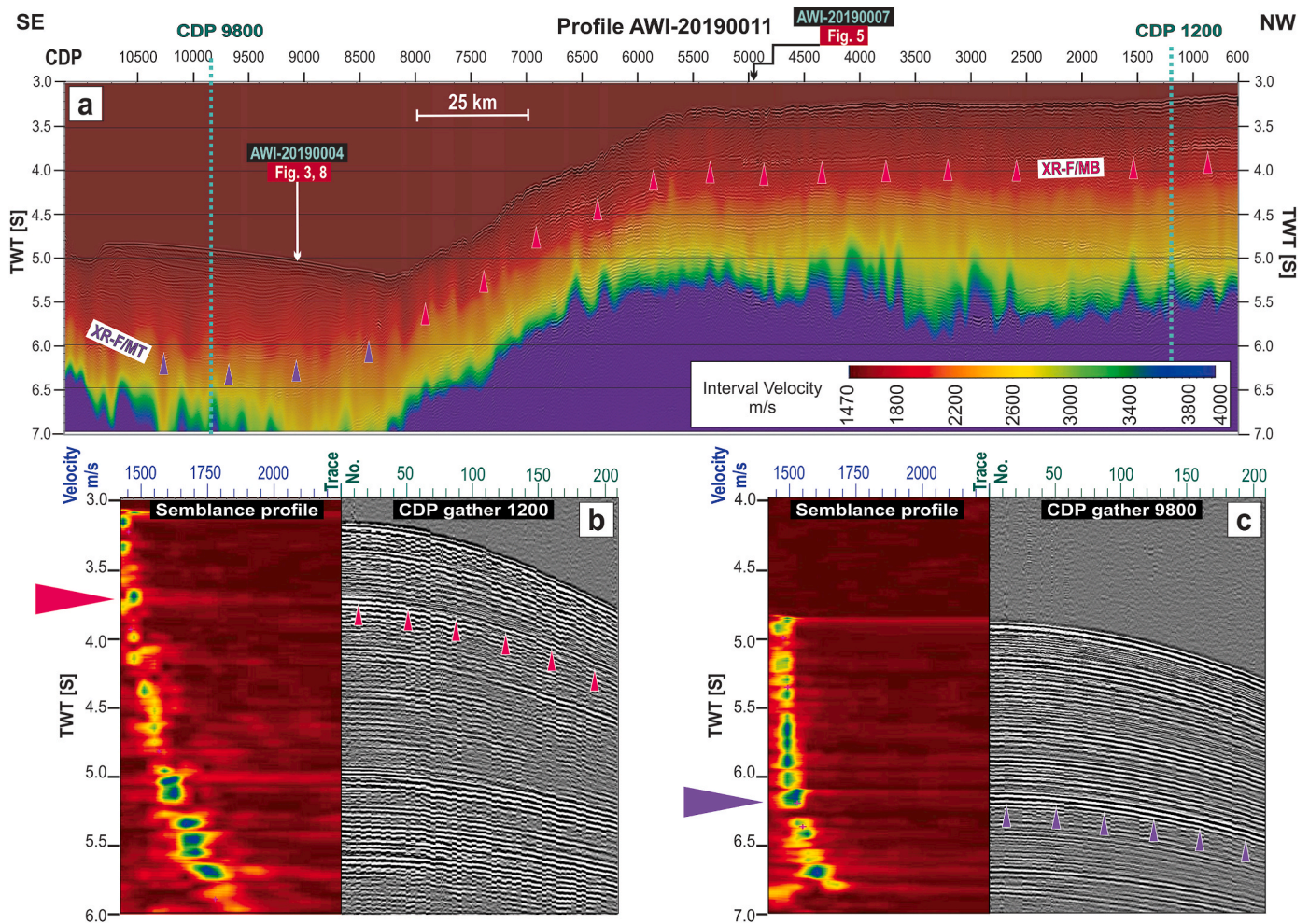
Fig. 7. (a) Seismic profile AWI-20190011. Location of profile is shown in Fig. 1b. The pink and purple triangles respectively mark the cross-cutting reflectors XR-F/MB and XR-F/MT (for details, see Section 4.1). Superimposed on the seismic profiles is the interval velocity section calculated from the seismic stacking velocity data, where the color scale gives the velocity values. Dashed cyan lines show the location of CDP 1200 and 9800. (b) and (c) respectively show the CDP gather 1200 and 9800 in gray scale (right) and the corresponding semblance profile (left). The pink and purple triangles respectively show the extent of reflectors XR-F/MB and XR-F/MT on the CDP gathers and semblance profiles. (for details, see Sections 4.2 and 6.2). Arrows show the location of crossing seismic profiles. (For interpretation of the references to color in this figure legend, the reader is referred to the Web version of this article.)

(Shipboard_Scientific_Party, 1980), the exposure of the Early-Middle Miocene horizon at the seafloor as observed on seismic data, and the abraded/hummocky texture of the seafloor on seismic (Fig. 3, AWI-20190004, CDPs 2500–5500) and Parasound profiles (Uenzelmann-Neben, 2019), together suggest that oceanic circulation on the Falkland/Malvinas Plateau has been relatively stable since at least the Middle-Late Miocene. Palaeoceanographic investigations using contouritic features across the MEB also concluded a relatively uniform intensity and pathway for LCDW since at least the Middle Miocene (Najjarifarizhendi and Uenzelmann-Neben, 2021). In today's oceanic setting, the oceanographic data place the velocity core of the LCDW at depths of 2000–3000 m, overspilling the F/MB and entering the Argentine basin (Arhan et al., 1999, 2002; Orsi et al., 1999).

We thus hypothesize that the large-scale reorganization of oceanic circulation following the opening of the Southern Ocean gateways and the onset and intensification of the ACC was responsible for the scouring and removal of at least 270 m of sediment across the F/MB. The prominent erosional phase in the Early-Middle Miocene may have driven the fossilization of the silica diagenetic fronts in the F/MB and the F/MT. We interpret the Early-Middle Miocene erosional surface, which seems to have defined the present-day seafloor at the F/MB, as the palaeo-seafloor in the F/MB and F/MT at the time of fossilization of silica diagenetic fronts.

6. Conclusions

Two high amplitude cross-cutting reflectors of normal (non-reversed) polarity are identified across the Falkland/Malvinas Basin and Trough using a set of new high-resolution seismic reflection profiles. Reflector XR-F/MB appears as a BSR, observed at about 500 msTWTbsf. In contrast, reflector XR-F/MT is an NBSR, which shows correlation with the geometry of a shallower reflector (reflector R-EMM), an Early-Middle Miocene unconformity that also shapes the seafloor in the F/MB.

The seismic and geometrical properties of reflectors XR-F/MB and XR-F/MT, together with lithological indications from DSDP Sites 327, 329, 330, and Site 511, allow these two cross-cutting reflectors to be associated with the Opal-A to Opal-CT transition zone. However, estimated temperatures at the present depth for these two reflectors based on regional geothermal gradients lie below the minimum temperatures known for the onset of silica diagenesis.

The geometrical characteristics of the two cross-cutting reflectors relative to the seafloor, as well as the presence of deformation features in strata between these reflectors and the seafloor reflector (polygonal faults and differential compaction folds) supports their interpretation as fossilized or arrested silica diagenetic fronts. The arrest of this boundary can be explained by a temperature drop due to widespread erosion and sediment removal by the action of abyssal water masses. It is
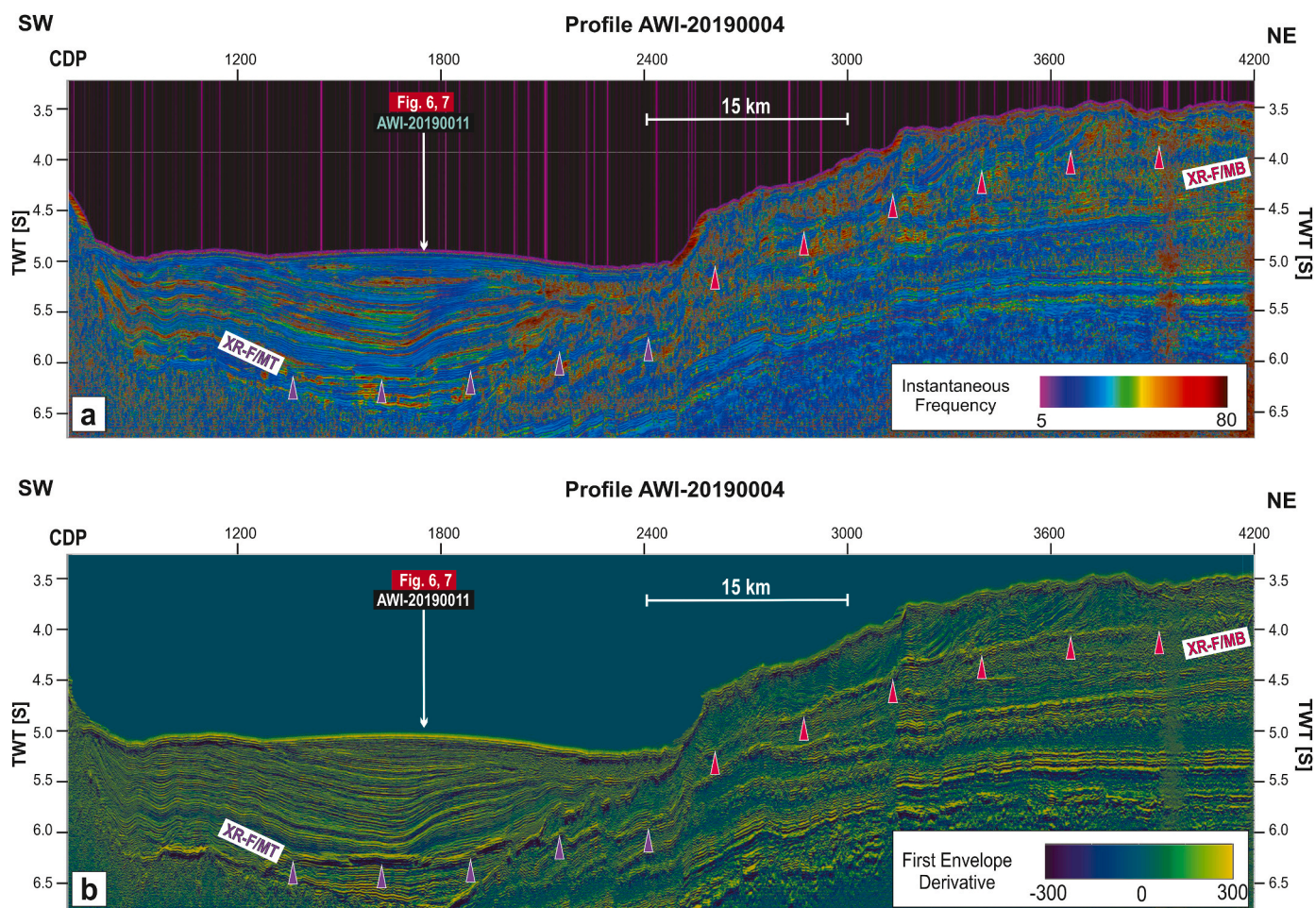
Fig. 8. Section from seismic profile AWI-20190004. Location of profile is shown in Fig. 1b. The pink and purple triangles respectively mark the cross-cutting reflectors XR-F/MB and XR-F/MT (for details, see Section 4.1). (a) and (b) Superimposed on the seismic profiles are respectively the instantaneous frequency and the first envelope derivative attribute section calculated from the seismic data, where the color scale gives the corresponding values (for details, see Sections 4.2 and 6.2). Arrows show the location of crossing seismic profiles. (For interpretation of the references to color in this figure legend, the reader is referred to the Web version of this article.)

hypothesized that the erosional action of intensified deep and bottom water masses at Early-Middle Miocene subsequent to Antarctic glaciations may have driven the fossilization of the diagenetic front in the study area. Erosion of a minimum of 270 m of overburden is estimated to have occurred, accounting for thermal conditions leading tor the fossilization of the silica diagenetic fronts.

7. Data References

Credit author statement

Gabriele Uenzelmann-Neben: Funding acquisition, Data curation, data preparation, Conceptualization, Writing – review & editing, **Banafsheh Najjarifarizhendi**: Data processing and interpretation, Conceptualization, Writing – original draft.

Declaration of competing interest

The authors declare that they have no known competing financial interests or personal relationships that could have appeared to influence the work reported in this paper.

Data availability

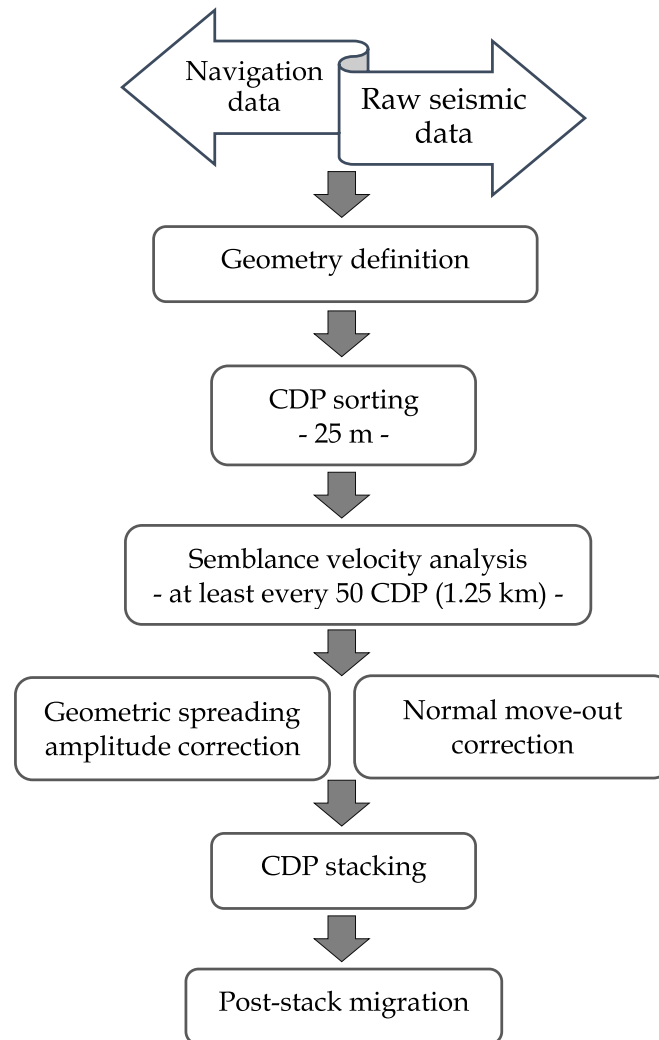Link to data is included in paper under "Data References"

Acknowledgments

Appendices.

Appendix A

Seismic processing Workflow.

Appendix B

Appendix B.1. is a review of the stratigraphic model of five units developed for the MEB by (Najjarifarizhendi and Uenzelmann-Neben, (2021)). Appendix B.2. presents modifications to the stratigraphic model by Najjarifarizhendi and Uenzelmann-Neben (2021) to extend the model towards the F/MB and F/MT. The modified model introduced units SU3′ and SU6, which are unique and restricted to the F/MB and F/MT

B.1. Seismic stratigraphy. Unit SU1 is bound by base reflector R-TB and top reflector R-JC, which respectively represent the top of the acoustic basement and the Jurassic-Cretaceous unconformity, and has semi-continuous to continuous middle-amplitude internal reflections (Figs. 3 and 5a). This unit wedges out on more elevated parts of the MEB (Fig. 3, AWI-20190001, CDPs 12000-14800), while it shows a variable thickness of up to 2000 ms TWT towards the F/MB. Unit SU1 fills basement troughs and follows the topography of the basement (Fig. 5a, CDPs 5000–12500).

Units SU2 and SU3 represent the Cretaceous strata, separated by a Middle Cretaceous unconformity (reflector R-MC) (Figs. 3 and 5a). Reflectors R-JC and R-MC respectively are the base and top boundaries of unit SU2. This unit has subparallel semi-continuous reflections within the F/MB and shows a constant thickness of ca. 250 ms TWT throughout the basin. Unit SU2 forms wedges up to 400 ms TWT thickon the shoulder of the MEB, which thin across more elevated parts of the MEB (Fig. 3, AWI-20190004, CDPs 6500–8170).

Unit SU2 is overlain by Unit SU3 with reflector R-MC at the base and reflector R-CT, a regional Cretaceous-Tertiary unconformity, at the top (Figs. 3 and 4). In the proximity of the MEB, Unit SU3 shows semi-continuous middle-to high-amplitude internal reflections and has its minimum thickness (less than 100 ms TWT) (Fig. 3, AWI-20190001, CDP 12000–14800). Within the F/MB, however, unit SU3 thickens strongly to more than 2000 ms

TWT and shows distinct internal structures (Fig. 3, AWI-20190004, CDP 3000–7000). These strata developed in a different depositional setting in the F/MB compared to the MEB. Therefore, the stratigraphic model is modified for seismic unit SU3 in the F/MB (Unit SU3'). For details see Appendix B.2.1 and Fig. 4.

Units SU4 and SU5 comprise the Cenozoic strata (Fig. 4). Reflector R-EO, which represents the Eocene-Oligocene unconformity, bounds Unit SU4 at the top (Figs. 4 and 5). Unit SU4 includes subparallel, semi-continuous to continuous, high-amplitude, undulated internal reflections which onlap Reflector R-CT at the base and are erosionally truncated at the top by Reflector R-EO (Fig. 5a, CDPs 2000–12000). Unit SU4 shows extreme thinning on the shoulder of the MEB (Fig. 3, AWI-20190001, CDPs 12000-13000) but is present in the F/MB with up to 400 ms TWT in thickness (Fig. 5a, CDPs 2000–12000).

Unit SU5 lies unconformably on reflector R-EO and is bounded at the top by the seafloor reflector (R–SF) (Figs. 3 and 4). This unit has its largest thickness (up to 1000 ms TWT) on top of the MEB. In general, it shows sub-horizontal to oblique, middle-to high-amplitude, high continuity, and wavy internal reflections (Figs. 3 and 5). Within the F/MB, Unit SU5 has similar reflection characteristics, with a thickness less than 350 ms TWT (Fig. 3, AWI-20190004, CDPs 3000–8000). Here, the Miocene subunits of unit SU5 (SU5-c and SU5-d) become indistinct and cannot be mapped on the seismic sections. In the southern parts of the F/MB, unit SU5 exhibits variable-amplitude and deformed reflections (Fig. 5a, CDPs 2000–4000). Reflector R-EMM, which represents the Early-Middle Miocene unconformity, truncates at the seafloor in the F/MB (Fig. 3, AWI-20190004, CDP 2400). Reflector R–SF has a very high-amplitude, continuous character and shows a rugged/abraded character in central and southern parts of the F/MB, whereas elsewhere it represents a smooth seafloor (Fig. 3, AWI-20190004, CDPs 2500–5500).

B.2. Modified Seismostratigraphic Model in F/MB and F/MT

In extending the seismostratigraphic model from the MEB by Najjarifarizhendi and Uenzelmann-Neben (2021) towards the F/MB and F/MT, two new units SU3' and SU6 have been introduced. Unit SU3' in F/MB, unlike its coeval unit SU3 on MEB includes thick strata including five distinct subunits. Unit SU6 in F/MT is a new unit unique in the F/MT, restricted to this area, including distinct mounded strata above the youngest unit SU5.

B.2.1. Unit SU3′, Reflectors R-MC to R-CT (Middle Cretaceous to Cretaceous-Tertiary). As with unit SU3 on the MEB, Unit SU3′ within the F/MB is bound at the base by reflector R-MC and at the top by reflector R-CT, in contrast, unit SU3′ shows distinct internal subunits (Fig. 3). Four previously undated (Middle -/Upper Cretaceous) unconformities R–UU1 to R–UU4 separate unit SU3′ into subunits SU3′-a, -b, -c, -d, and -e (Figs. 3 and 4).

Subunit SU3′-a is bound by base reflector R-MC and top reflector R–UU1 (Figs. 3 and 4). Reflector R–UU1 has a sub-horizontal, semi-continuous, low-amplitude character (Fig. 3, AWI-20190004, CDPs 5000–8000). Subunit SU3′-a forms wedges up to 800 ms TWT thick, on the eastern and northern margins of the F/MB. Elsewhere in the F/MB, this subunit has a constant thickness of ca 100 ms TWT (Fig. 3). Subunit SU3′-a displays sub-horizontal, semi-continuous, low-amplitude, widely-spaced internal reflections, which are erosionally truncated at the top by reflector R–UU1.

Reflector R–UU2, which bounds subunit SU3′-b at the top, is a middle-to high-amplitude, semi-continuous to discrete reflector (Fig. 3). Subunit SU3′-b, which unconformably lies on reflector R–UU1, in general is seismically opaque, but occasionally includes medium-amplitude, discrete, and widely-spaced reflectors. It forms wedges in northern parts of the F/MB with up to 1000 ms TWT thickness. In central parts of the M/FB, subunit SU3′-b includes lens-shaped structures with minimum and maximum thicknesses of respectively ca. 150 and 1000 ms TWT, which are truncated on the top by reflector R–UU2 (Fig. 3, AWI-20190004, CDPs 3000–6000).

Subunit SU3′-c unconformably lies on base reflector R–UU2 and is bound at the top by reflector R–UU3, which is a sub-horizontal, high-amplitude, continuous reflector across the F/MB (Fig. 3). This subunit shows middle-to high-amplitude, semi-continuous internal reflections and a constant thickness of ca. 400 ms TWT across the F/MB (Fig. 3). Southwards towards the F/MT, subunit SU3′-c can reach a thickness of up to 700 ms TWT. Internal reflections of SU3′-c are erosionally truncated in northern and eastern parts of the F/MB by reflector R-CT (Fig. 3, AWI-20190004, CDPs 6000–7000), and in the southern F/MB by the younger unconformity R–UU4 (Fig. 3, AWI-20190004, CDP 2500–3500).

Subunit SU3′-d is bound at the base and top by Reflectors R–UU3 and R–UU4 respectively. The latter is a sub-horizontal, low-to middle-amplitude, semi-continuous reflector within the F/MB (Fig. 3). Subunit SU3′-d shows mainly chaotic internal reflections overall in the F/MB, except for the eastern and western F/MB where it shows oblique, high-amplitude, semi-continuous internal reflections (Fig. 3, AWI-20190004, CDPs 3300–3700). Here, internal reflectors show lateral displacement towards the south, where the upper reflectors downlap onto lower reflectors. Subunit SU3′-d has a relatively constant thickness of ca. 350 ms TWT across the F/MB. Reflections of this subunit are truncated by reflector R-CT in eastern and northern parts of the F/MB (Fig. 3, AWI-20190004, CDPs 5400–5800). In the southern parts of the F/MB, internal reflections of SU3′-d terminate against reflector R–UU4 (Fig. 3, AWI-20190004, CDPs 3100–3400).

Reflectors R-CT and R–UU4 respectively, form the top and base reflector of subunit SU3′-e. Within the F/MB, reflector R-CT shows a twofold character. In northern and eastern parts, reflector R-CT is a subhorizontal, high-amplitude, continuous reflector (Fig. 3, AWI-20190004, CDPs 2400–5400), whereas elsewhere in the basin it shows a tangential, middle-amplitude, wavy, and highly scattered reflection (Fig. 3, AWI-20190004, CDPs 6000–8100). The lower part of this unit exhibits middle-amplitude, semi-continuous to discrete, widely-spaced reflections; towards the upper part, reflections of SU3′-e have disturbed and wavy character (Fig. 3, AWI-20190004, CDPs 2600–4600). SU3′-e shows extreme thinning in northern and eastern parts of F/MB. It shows variable thickness elsewhere within the F/MB, where it forms cone-shaped features truncated on the top by reflector R-CT (Fig. 3, AWI-20190004, CDPs 3500–5200).

B.2.2. Seismic unit SU6, Reflectors R-EMM to Seafloor (Early-Middle Miocene to Recent). Bounding reflectors of Units SU1 and SU2, reflectors R-TB, R-JC, and R-MC, are very well trackable southwards from the F/MB towards the F/MT as they plunge below the northern margin of the F/MT (Fig. 3, AWI-20190004, CDPs 2000–3000). For the Cretaceous Unit SU3' and Tertiary Unit SU4, however, the bounding reflectors R-CT and R-EO become indistinct in the southernmost extremity of the F/MB and are hardly trackable into the F/MT (Fig. 3, AWI-20190004, CDPs 2500–2900). Units SU1-SU4 show tilting and faulting in the F/MT, and younger F/MT fill lies unconformably on these strata on the northern flank of the F/MT (Fig. 3, AWI-20190004, CDPs 2000–2500).

The sedimentary sequence resolved in the F/MT cannot be dated with confidence, however partial tracking of reflector R-EO from the F/MB into the F/MT locates it below this sedimentary sequence on the northern flank of the F/MT (Fig. 5a, CDP 1900). This provides a hint on the age of the filling strata being younger than the Eocene-Oligocene, suggesting that these strata are coeval to unit SU5 in F/MB. These strata however show different seismic characteristics compared to those of unit SU5, since they build up as a thick and conforming package. Therefore, the seismo-stratigraphic model is expanded to include an additional unit SU6 with three subunits.

Subunit SU6-a includes mostly horizontal and sub-horizontal internal reflections which onlap the acoustic basement on the southern flank of the M/FT and the southward dipping strata of units SU3′-SU5 on the northern flank (Fig. 3, AWI-20190004, CDPs 700–2400 and Fig. 6c). This subunit occasionally includes transparent strata. Reflector R-EMM, which is an Early-Middle Miocene erosional unconformity, truncates reflections of subunit SU6-a at the top (Fig. 3). Reflections of subunit SU6-a show high-continuity, middle-to high-amplitude, and middle-to high-frequency reflections. This subunit shows its maximum thickness of up to 1200 ms TWT in the central section of the F/MT, while it thins and pinches out on the southern and northern flanks and occasionally includes moats and mounded sediment bodies (Fig. 6c).

An undated erosional unconformity (hereafter called R–UU5) bounds subunit SU6-b at the top. Reflector R–UU5 is a continuous, middle-amplitude reflector that truncates reflections of subunit SU6-a (Fig. 3, AWI-20190004, CDPs 700–2400). Reflections of subunit SU6-b lie sub-parallel to but occasionally onlap reflector R-EMM (Fig. 6c, CDP 8600). Subunit SU6-b shows a variable thickness across the F/MT, ranging from less than 100 ms TWT towards the northern and southern F/MT flanks to more than 300 ms TWT in central parts of F/MT. This subunit has sub-parallel, continuous, middle-to high-amplitude internal reflections and includes moats close to the northern (Fig. 3, CDP 8600) and southern (Fig. 6c, CDP 10400) flanks of the F/MT that show a gradual up-dip migration.

Subunit SU6-c is the youngest subunit in the F/MT. It lies sub-parallel to the base reflector R–UU5 and is bound at the top by the seafloor reflector (R–SF). This unit has sub-parallel, continuous, low-to middle-amplitude internal reflections, which are truncated by reflector R–SF. This subunit forms a well-developed symmetric mounded sediment body in central parts of the F/MT, which reaches a thickness of up to 250 ms TWT and wedges out on the southern and northern flanks of the F/MT. Subunit SU6-c includes moats at the flanks of the F/MT which extend up-dip and are seen at the seafloor (Fig. 6c, CDP 1150–1800).

References

Allen, C.S., Pike, J., Pudsey, C.J., Leventer, A., 2005. Submillennial variations in ocean conditions during deglaciation based on diatom assemblages from the southwest Atlantic. Paléo 20 (2).

Allen, C.S., Pike, J., Pudsey, C.J., 2011. Last glacial-interglacial sea-ice cover in the SW Atlantic and its potential role in global deglaciation. Quat. Sci. Rev. 30 (19–20), 2446–2458.

Aminzadeh, F., Dasgupta, S.N., 2013. Chapter 3 - fundamentals of petroleum geophysics. In: Aminzadeh, F., Dasgupta, S.N. (Eds.), Developments in Petroleum Science. Elsevier, pp. 37–92.

Arhan, M., Heywood, K.J., King, B.A., 1999. The deep waters from the Southern Ocean at the entry to the Argentine Basin. Deep-Sea research II 46, 475–499.

Arhan, M., Naveira Garabato, A.C., Heywood, K.J., Stevens, D.P., 2002. The antarctic circumpolar current between the Falkland Islands and south Georgia. J. Phys. Oceanogr. 32, 1914–1931.

Baristeas, N., Anka, Z., di Primio, R., Rodriguez, J.F., Marchal, D., Dominguez, F., 2012. Distribution of hydrocarbon leakage indicators in the Malvinas Basin, offshore Argentine continental margin. Mar. Geol. 332–334, 56–74.

Barker, P., 1977. Correlations between Sites on the Eastern Falkland Plateau by Means of Seismic Reflection Profiles, vol. 36. LEG (DSDP).

Barker, P.F., Thomas, E., 2004. Origin, signature and palaeoclimatic influence of the antarctic circumpolar current. Earth Sci. Rev. 66, 143–166.

Ben Avraham, Z., Hartnady, C.H.J., Kitchin, K.A., 1997. Structure and tectonics of the Agulhas-Falkland fracture zone. Tectonophysics 282, 83–98.

Berndt, C., Bünz, S., Clayton, T., Mienert, J., Saunders, M., 2004. Seismic character of bottom simulating reflectors: examples from the mid-Norwegian margin. Mar. Petrol. Geol. 21, 723–733.

Bohrmann, G., Spieß, V., Hinze, H., Kuhn, G., 1992. Reflector "Pc" a prominent feature in the Maud Rise sediment sequence (eastern Weddell Sea): occurrence, regional distribution and implications to silica diagenesis. Mar. Geol. 106, 69–87.

Brekke, H., Dahlgren, S., Nyland, B., Magnus, C., 1999. The prospectivity of the Vøring and Møre basins on the Norwegian Sea continental margin. Geological Society, London, Petroleum Geology Conference series 5 (1), 261–274.

Bünz, S., Mienert, J., Berndt, C., 2003. Geological controls on the Storegga gas-hydrate system of the mid-Norwegian continental margin. Earth Planet Sci. Lett. 209, 291–307.

Carcione, J., Picotti, S., 2006. P-Wave Seismic Attenuation by Slow-Wave Diffusion: Effects of Inhomogeneous Rock Properties: Geophysics, vol. 71. https://doi.org/10.1190/1.219452. O1–O8.

Ciesielski, P.F., Wise Jr., S.W., 1977. Geologic history of the Maurice Ewing Bank of the Falkland plateau (southwest atlantic sector of the Southern Ocean) based on piston and drill cores. Mar. Geol. 25, 175–207.

Cunningham, A.P., 1999. Geophysical Investigations of the North Scotia Ridge. Unpublished PhD thesis, University of London, London, England.

Cunningham, A.P., Barker, P.F., 1996. Evidence for westward-flowing Weddell Sea Deep water in the Falkland trough, western South Atlantic. Deep-Sea Res. I 43 (5), 643–654.

Davies, R.J., 2005. Differential compaction and subsidence in sedimentary basins due to silica diagenesis: a case study. Geol. Soc. Am. Bull. 117, 1146–1155.

Davies, R., Cartwright, J., 2002. A fossilized Opal A to Opal C/T transformation on the northeast Atlantic margin: support for a significantly elevated palaeogeothermal gradient during the Neogene? Basin Res. 14, 467–486.

Davies, R.J., Clark, I.R., 2006. Submarine slope failure primed and triggered by silica and its diagenesis. Basin Res. 18, 339–350.

Davies, R., Bell, B.R., Cartwright, J.A., Shoulders, S., 2002. Three-dimensional seismic imaging of Paleogene dike-fed submarine volcanoes from the northeast Atlantic margin. Science 30, 223–226.

Davies, R.J., Ireland, M.T., Cartwright, J.A., 2009. Differential compaction due to the irregular topology of a diagenetic reaction boundary: a new mechanism for the formation of polygonal faults. Basin Res. 21, 354–359.

Dick, H.v.d., Rullkotter, J., Welte, D.H., 1983. Content, Type, and Thermal Evolution of Organic Matter in Sediments from the Eastern Falkland Plateau. Deep Sea Drilling Project. Leg 71.

Domenico, S.N., 1977. Elastic properties of unconsolidated porous sand reservoirs. Geophysics 42, 1339–1368.

Dummann, W., Steinig, S., Hofmann, P., Flögel, S., Osborne, A.H., Frank, M., Herrle, J.O., Bretschneider, L., Sheward, R.M., Wagner, T., 2020. The impact of Early Cretaceous gateway evolution on ocean circulation and organic carbon burial in the emerging South Atlantic and Southern Ocean basins. Earth Planet Sci. Lett. 530, 115890.

Fetter, A.F.H., Matano, R.P., 2008. On the origins of the variability of the Malvinas Current in a global, eddy-permitting numerical simulation. J. Geophys. Res. C113.

Geletti, R., Busetti, M., 2011. A double bottom simulating reflector in the western Ross Sea, Antarctica. J. Geophys. Res. Solid Earth 116.

Grützner, J., Mienert, J., 1999. Physical property changes as a monitor of pelagic carbonate diagenesis: an empirically derived diagenetic model for Atlantic Ocean basins. AAPG (Am. Assoc. Pet. Geol.) Bull. 83, 1485–1501.

Guerin, G., Goldberg, D., 2002. Sonic waveform attenuation in gas hydrate-bearing sediments from the Mallik 2L-38 research well, Mackenzie Delta, Canada. J. Geophys. Res. Solid Earth 107. EPM 1-1-EPM 1-11.

Hein, J.R., Scholl, D.W., Barron, J.A., Jones, M.G., Miller, J., 1978. Diagenesis of late Cenozoic diatomaceous deposits and formation of the bottom simulating reflector in the southern Bering Sea. Sedimentology 25, 155–181.

Hesse, R., 1988. Diagenesis #13. Origin of chert: diagenesis of biogenic siliceous sediments. Geosci. Can. 15, 171–192.

Isaacs, C.M., 1981. Porosity Reduction during Diagenesis of the Monterey Formation. Santa Barbara coastal area, California.

Johnston, D.H., 2010. Methods and Applications in Reservoir Geophysics. Society of Exploration Geophysicists.

Kastner, M., Keene, J., Gieskes, J., 1977a. Diagenesis of siliceous oozes—I. Chemical controls on the rate of opal-A to opal-CT transformation—an experimental study. Geochem. Cosmochim. Acta 41, 1041–1059.

Kastner, M., Keene, J.B., Gieskes, J.M., 1977b. Diagenesis of siliceous oozes—I. Chemical controls on the rate of opal-A to opal-CT transformation—an experimental study. Geochem. Cosmochim. Acta 41, 1041–1059.

Kim, H.-J., Jou, H.-T., Kang, S.-G., Lee, G.H., Yi, B.Y., Yoo, D.-G., Ryu, B.-J., Shin, C., 2013. Seismic characterization and imaging of a gas hydrate deposit in the western part of the Ulleung Basin, the East Sea (Japan Sea). Mar. Petrol. Geol. 47, 214–221.

Koenitz, D., White, N., McCave, I.N., Hobbs, R., 2008. Internal structure of a contourite drift generated by the Antarctic Circumpolar Current. G-cubed 9 (n/a-n/a).

Kuramoto, S., Tamaki, K., Langseth, M., Nobes, D., Tokuyama, H., Pisciotto, K., Taira, A., 1992. Can Opal-A/opal-CT BSR Be an Indicator of the Thermal Structure of the Yamato Basin, p. 73. Japan Sea. Age 794.

Kvenvolden, K.A., 1994. Natural gas hydrate occurrence and issues. Ann. N. Y. Acad. Sci. 715, 232–246.

Langseth, M., Ludwig, W., 1983. A Heat-Flow Measurement on the Falkland Plateau, vol. 71. Initial Reports of the Deep Sea Drilling Project, pp. 299–303.

Lee, M.W., 2004. Elastic velocities of partially gas-saturated unconsolidated sediments. Mar. Petrol. Geol. 21, 641–650.

Lodolo, E., Camerlenghi, A., Brancolini, G., 1993. A bottom simulating reflector on the South Shetland margin, Antarctic Peninsula. Antarct. Sci. 5, 207–210, 02.

Lorenzo, J.M., Mutter, J.C., 1988. Seismic stratigraphy and tectonic evolution of the Falkland/Malvinas Plateau. Rev. Bras. Geociencias 18, 191–200.

Ludwig, W.J., 1983. Geologic framework of the Falkland plateau. In: Ludwig, W.J., Krasheninnikov, V.A., et al (Eds.), Initial Reports DSDP. U.S. Govt. Printing Office, Washington, pp. 281–293.

Shipboard Scientific Party, 1980. Site 511. In: Ludwig, W.J., Krasheninnikov, V.A., et al (Eds.), Initial Reports DSDP. U.S. Govt. Printing Office, Washington, pp. 21–109.

Meadows, D., Davies, R.J., 2010. The limited suitability of silica diagenetic boundaries as isothermal markers: insights from seismic reflection imaging, Offshore Sakhalin, Russian Far East. Mar. Petrol. Geol. 27, 1028–1039.

Minshull, T.A., Keddie, A., 2010. Measuring the geotherm with gas hydrate bottom-simulating reflectors: a novel approach using three-dimensional seismic data from the eastern Black Sea. Terra. Nova 22, 131–136.

Muza, J.P., Williams, D.F., Wise Jr., S.W., 1980. Paleogene oxygen isotope record for Deep Sea Drilling sites 511 and 512, subantarctic South Atlantic ocean: paleotemperatures, paleoceanographic changes, and the eocene/oligocene boundary event. In: Ludwig, W.J., Krasheninnikov, V.A., et_al (Eds.), Initial Reports DSDP. U.S. Govt. Printing Office, Washington, pp. 409–422.

Najjarifarizhendi, B., Uenzelmann-Neben, G., 2021. Footprints of palaeocurrents in sedimentary sequences of the cenozoic across the Maurice Ewing Bank. Mar. Geol. 438.

Neagu, R.C., Cartwright, J., Davies, R., Jensen, L., 2010. Fossilisation of a silica diagenesis reaction front on the mid-Norwegian margin. Mar. Petrol. Geol. 27, 2141–2155.

Nicholson, U., Stow, D., 2019. Erosion and deposition beneath the subantarctic front since the early Oligocene. Sci. Rep. 9, 9296.

Nobes, D.C., Murray, R.W., Kuramoto, S.i., Pisciotto, K.A., Holler, P., 1992. Impact of Silica Diagenesis on Physical Property Variations. In: Proceedings of the Ocean Drilling Program, Scientific Results. Ocean Drilling Program, College Station, pp. 3–23.

Nouzé, H., Cosquer, E., Collot, J., Foucher, J.-P., Klingelhoefer, F., Lafoy, Y., Géli, L., 2009. Geophysical characterization of bottom simulating reflectors in the Fairway Basin (off New Caledonia, Southwest Pacific), based on high resolution seismic profiles and heat flow data. Mar. Geol. 266, 80–90.

Ohde, A., Otsuka, H., Kioka, A., Ashi, J., 2018. Distribution and depth of bottom-simulating reflectors in the Nankai subduction margin. Earth Planets Space 70, 60.

Orsi, A.H., Whitworth, T., Nowlin, W.D., 1995. On the meridional extent and fronts of the Antarctic Circumpolar Current. Deep Sea Res. Oceanogr. Res. Pap. 42, 641–673.

Orsi, A.H., Johnson, G.C., Bullister, J.L., 1999. Circulation, mixing, and production of antarctic bottom water. Prog. Oceanogr. 43, 55–109.

Pérez, L.F., De Santis, L., McKay, R.M., Larter, R.D., Ash, J., Bart, P.J., Böhm, G., Brancatelli, G., Browne, I., Colleoni, F., Dodd, J.P., Geletti, R., Harwood, D.M., Kuhn, G., Sverre Laberg, J., Leckie, R.M., Levy, R.H., Marschalek, J., Mateo, Z., Naish, T.R., Sangiorgi, F., Shevenell, A.E., Sorlien, C.C., van de Flierdt, T., Scientists, I.O.D.P.E., 2021. Early and middle Miocene ice sheet dynamics in the Ross Sea: results from integrated core-log-seismic interpretation. GSA Bulletin 134. (1–2), 348–370.

Popescu, I., De Batist, M., Lericolais, G., Nouzé, H., Poort, J., Panin, N., Versteeg, W., Gillet, H., 2006. Multiple bottom-simulating reflections in the Black Sea: potential proxies of past climate conditions. Mar. Geol. 227, 163–176.

Richards, P.C., Gatliff, R.W., Quinn, M.F., Fannin, N.G.T., Williamson, J.P., 1996. The Geological Evolution of the Falkland Islands Continental Shelf, vol. 108. Geological Society, London, Special Publications, pp. 105–128.

Rivas, L., Pérez Panera, J.P., Cusminsky, G.C., 2018. Pliocene - holocene calcareous nannofossils from the Malvinas trough, southwestern atlantic ocean. In: Reunión de Comunicaciones de la Asociación Paleontológica Argentina. Puerto Madryn, p. 92.

Roaldset, E., Wei, H., 1997. Silica-phase transformation of opal-A to opal_CT to quartz, Part I: An experimental diagenetic approach to natural observations. Prepared for submittal to AAPG.

Rundberg, Y., 1989. ertiary sedimentary history and basin evolution of the Northern North Sea *between 6U'N and 6Z'N*, PhD Thesis. University of Trondheim, , Norway.

Sain, K., Minshull, T., Singh, S., Hobbs, R., 2000. Evidence for a thick free gas layer beneath the bottom simulating reflector in the Makran accretionary prism. Mar. Geol. 164, 3–12.

Saito, T., Burckle, L.H., Hays, J.D., 1974. Implications of Some Pre-quaternary Sediment Cores and Dredgings.

Scher, H.D., Martin, E.E., 2006a. Timing and climatic consequences of the opening of Drake Passage. Science 312, 428–430.

Scher, H.D., Martin, E.E., 2006b. Timing and climatic consequences of the opening of Drake Passage. Science 312, 428–430.

Schreider, A.A., Mazo, E.L., Bulychev, A.A., Kulikova, M.P., Gilod, D.A., Schreider, A.A., Boïko, A.N., 2010. Peculiarities of the earth's crust sedimentary layer structure in the Falkland basin. Oceanology 50, 961–970.

Shedd, W., Boswell, R., Frye, M., Godfriaux, P., Kramer, K., 2012. Occurrence and nature of "bottom simulating reflectors" in the northern Gulf of Mexico. Mar. Petrol. Geol. 34, 31–40.

Shipboard_Scientific_Party, 1974a. Site 327. In: Barker, P.F., Dalziel, I., Wise Jr., S.W. (Eds.), Initail Reports DSDP. US Government Printing, Washington, pp. 27–86.

Shipboard_Scientific_Party, 1974b. Site 329. In: Barker, P.F., Dalziel, I., Wise Jr., S.W. (Eds.), Initial Reports DSDP. US Government Printing, Washington, pp. 143–206.

Shipboard_Scientific_Party, 1974c. Site 330. In: Barker, P.F., Dalziel, I., Wise Jr., S.W. (Eds.), Initail Reports DSDP. US Government Printing, Washington, pp. 207–257.

Shipboard_Scientific_Party, 1977. Evolution of the southwestern atlantic ocean basin: results of Leg 36, Deep Sea Drilling Project. In: Barker, P.F., Dalziel, I., Wise Jr., S.W., et_al (Eds.), Initial Reports DSDP. U.S. Govt. Printing Office, Washington, pp. 993–1014.

Shipley, T.H., Houston, M.H., Buffler, R.T., Shaub, F.J., Mcmillen, K.J., Laod, J.W., Worzel, J.L., 1979. Seismic evidence for widespread possible gas hydrate horizons on continental slopes and Rises1. AAPG (Am. Assoc. Pet. Geol.) Bull. 63, 2204–2213.

Sloan Jr., E.D., 1998. Clathrate Hydrates of Natural Gases, Revised and Expanded. CRC press.

Somoza, L., León, R., Medialdea, T., Pérez, L.F., González, F.J., Maldonado, A., 2014. Seafloor mounds, craters and depressions linked to seismic chimneys breaching fossilized diagenetic bottom simulating reflectors in the central and southern Scotia Sea, Antarctica. Global Planet. Change 123, 359–373. Part B.

Subrahmanyam, D., Rao, P., 2008. Seismic Attributes-A Review, 7th International Conference & Exposition on Petroleum Geophysics, pp. 398–404. Hyderabad.

Taner, M.T., 2001. Seismic attributes. CSEG recorder 26, 48–56.

Taner, M., Koehler, F., Sheriff, R., 1979. Complex seismic trace analysis: Geophysics. Geophysics 1041–1063.

Taner, M.T., Scheuelke, J., O'Doherty, R., Baysal, E., 1994. Seismic attributes revisited. SEG expanded abstract. Annual International Meeting 1104–1106.

Taylor, M., Dillon, W.P., Pecher, I., 2000. Trapping and migration of methane associated with the gas hydrate stability zone at the Blake Ridge Diapir: new insights from seismic data. Mar. Geol. 164, 79–89.

Uenzelmann-Neben, G., 2019. Onset and Modifications in Intensity and Pathways of Water Mass Exchange between the Southeast Pacific and the South Atlantic with Focus on the Falkland Plateau, Northern Scotia Ridge and the West Georgia Basin, Cruise No. MSM81, February 2 2019-March 15 2019, Valparaiso (Chile) - Montevideo (Uruguay. MARIA S. MERIAN-Berichte, Bonn, p. 30.

Uenzelmann-Neben, G., Weber, T., Grützner, J., Thomas, M., 2017. Transition from the Cretaceous ocean to Cenozoic circulation in the western South Atlantic — a twofold reconstruction. Tectonophysics 716, 225–240.

Vanneste, M., Mienert, J., Guidard, S., partners, H.I., 2002. Arctic'' Gas Hydrates Offshore Western Svalbard, Norway. In: Proceedings of the 4th International Conference on Gas Hydrates, pp. 19–23. Yokohama, Japan.

Varkouhi, S., Cartwright, J.A., Tosca, N.J., 2020. Anomalous compaction due to silica diagenesis — textural and mineralogical evidence from hemipelagic deep-sea sediments of the Japan Sea. Mar. Geol. 426, 106204.

Varkouhi, S., Cartwright, J.A., Tosca, N.J., Papineau, D., 2022. Arrested versus active silica diagenesis reaction boundaries—a review of seismic diagnostic criteria. Basin Res. 34, 640–661.

Volpi, V., Camerlenghi, A., Hillenbrand, C.-D., Rebesco, M., Ivaldi, R., 2004. The effects of biogenic silica on sediment compaction and slope stability on the pacific margin of the Antarctic Peninsula. Basin Res. 15 (3), 339–363.

Whalley, E., 1980. Speed of longitudinal sound in clathrate hydrates. J. Geophys. Res. Solid Earth 85, 2539–2542.

Wise Jr., S.W., 1972. Chemically precipitated sedimentary cristobalite and the origin of chert. Eclogae Geol. Helv. 65, 157–163.

Wrona, T., Jackson, C.A.L., Huuse, M., Taylor, K.G., 2017. Silica diagenesis in Cenozoic mudstones of the North Viking Graben: physical properties and basin modelling. Basin Res. 29, 556–575.

Yilmaz, Ö., 2001. Seismic Data Analysis: Processing, Inversion, and Interpretation of Seismic Data. Society of exploration geophysicists.